Numerical study of homogeneous bubbly flow: Influence of the inlet conditions to the hydrodynamic behavior

D. Darmana [a,1], N.G. Deen [a,*], J.A.M. Kuipers [a], W.K. Harteveld [b,2], R.F. Mudde [b]

[a] Fundamentals of Chemical Reaction Engineering, Faculty of Science and Technology, University of Twente, P.O. Box 217, 7500 AE Enschede, The Netherlands
[b] Multi-Scale Physics, Faculty of Applied Sciences, Delft University of Technology, The Netherlands

ARTICLE INFO

ABSTRACT

This paper discusses the role of the gas injection pattern on the large scale structures in a homogeneous pseudo-2D bubble column operated at relatively high gas hold-ups up to 8%. Seven cases with different inlet configuration have been studied experimentally by Harteveld et al. Each of these cases has been simulated using a (parallel) Euler–Lagrange model developed by Darmana et al. The presence of coherent structures for both uniform and non-uniform gas injection is studied. Furthermore, the influence of the gas injection pattern on the dynamics is investigated, while the statistical (average and fluctuating) quantities are compared with the PIV/PTV and LDA measurement data of Harteveld et al. The results show that the model resembles the observed experimental flow structures to a large extent.

© 2009 Elsevier Ltd. All rights reserved.

1. Introduction

In the chemical industry bubble columns are often used because of their simple construction and operation, good heat and mass transfer properties and isothermal conditions of operation. The flow in a bubble column is complex and not yet well understood despite the extensive research devoted to this topic. Based on the flow rates of the gas phase, two typical flow regimes can be distinguished. At low gas flow rates, the homogeneous regime is found, which is characterized by uniformly distributed bubbles and the absence of large scale liquid circulation. On the other hand, when high flow rates are utilized the heterogeneous regime is found, displaying non-uniformly distributed bubbles and large scale liquid circulation.

From a practical point of view a bubble column operated in the homogeneous regime with relatively high gas hold-up and a small uniform bubble size is often desirable to get plug flow and maximum residence time. It is rather difficult however, to generate a uniform flow especially at relatively high gas hold-ups, since the coalescence rate normally increases under these conditions. Due to coalescence a non-uniform bubble size distribution will be generated, which will induce non-uniformity of the flow behavior.

One of the key elements to obtain a homogeneous bubbly flow system is the employment of uniform injection of relatively small bubbles as suggested by Harteveld et al. (2004). They showed

experimentally that a uniform flow without large scale vortical structures and circulation patterns is obtained with very uniform injection; and additionally that the vortical structures and circulation can be re-obtained by introduction of non-aerated zones. Their experimental results provide valuable data that can be used to validate CFD models and improve our understanding of the role of the bubble size and of the sparger with respect to the hydrodynamics and prevailing flow structures in bubble columns.

A significant amount of computational work has been performed over the last decade to reproduce the dynamics of the large scale circulation and vortical structures computationally. In numerical simulations typically lab-scale bubble columns are considered at relatively low superficial gas velocities with a localized gas distributor area at the base of the column (Becker et al., 1994; Delnoij et al., 1997; Delnoij et al., 1999; Sokolichin et al., 1997; Mudde and Simonin, 1999; Sokolichin and Eigenberger, 1999; Deen et al., 2001; Borchers et al., 1999; Oey et al., 2003; Buwa and Ranade, 2003; Darmana et al., 2004; Sokolichin et al., 2004; Darmana et al., 2005a; Darmana et al., 2005b; Buwa et al., 2006; Darmana et al., 2007). This type of bubble column operation will create a bubble plume which is meandering irregularly and automatically implies non-uniformity of the gas hold-up throughout the column.

Using either Euler–Euler or Euler–Lagrange models some authors like Laín et al. (1999), Deen et al. (2001), Laín et al. (2002), Buwa and Ranade (2003), Darmana et al. (2004), Monahan et al. (2005), Chen et al. (2005a), Chen et al. (2005b) and Buwa et al. (2006) reported that using the widely accepted closure correlations (a.o. closures proposed by Tomiyama et al. (2002, 1995)) both the dynamics and time-averaged behavior in a partially aerated

* Corresponding author. Tel.: +31 53 489 4138; fax: +31 53 489 2882.
  E-mail address: N.G.Deen@utwente.nl (N.G. Deen).
[1] Present address: SINTEF Materials and Chemistry, Trondheim, Norway.
[2] Present address: Shell Global Solutions, Amsterdam, The Netherlands.

bubble column at low gas hold-up can be reproduced very well. As most of the closures are empirically obtained from experiments involving single bubbles (or droplets), their applicability to systems with high gas hold-ups is questionable. On the other hand, hardly any correlation is available in literature which takes into account the effect of the local gas hold-up. One of the works in this research area (the simulation results by Behzadi et al. (2004)) suggests that using drag and lift correlations, which account for the elevated dispersed phase fraction, does not yield satisfactory results.

In this paper, the experimental cases studied by Harteveld et al. (2004) are simulated by means of a CFD model. The CFD code used in the present study is the parallel version of the transient three-dimensional Euler–Lagrange model developed by Darmana et al. (2006) supplemented with the force closures proposed by Tomiyama et al. (2002), Tomiyama et al. (1997), Tomiyama et al. (1995). The presence of coherent structures for both uniform and non-uniform gas injectors is studied together with the influence of the gas injection pattern on the dynamics. In addition the statistical (average and fluctuating) quantities are compared with the PIV/PTV and LDA measurement data of Harteveld et al. (2004), who performed a large series of experiments in a bubble column with a well defined sparger. With the use of such a sparger an

almost-uniform bubbly flow ia attained, which is rather difficult to model accurately. That is, more subtle effects are at play than in the case of one central injector. This study in particular is meant to further validate the developed Euler–Lagrange model and the underlying closures. It is used to investigate the applicability of both the model and the applied closures to simulate bubble columns that are operated in a (homogeneous) regime with high gas hold-ups up to 8%.

2. Experiments

The experimental data used in the present study are taken from the work of Harteveld et al. (2004) and Harteveld (2005) and will be briefly explained here for the sake of clarity.

2.1. Experimental setup

The pseudo-2D bubble column used in the experiments was a 50% down-scaled version of that used by Becker et al. (1994). A schematic overview of the experimental setup is given in Fig. 1(a). The column has a width of 24.3 cm, depth of 4.05 cm and a height of 99 cm. The sparger for this column is made of 95 needles arranged in a triangular pattern with a distance between
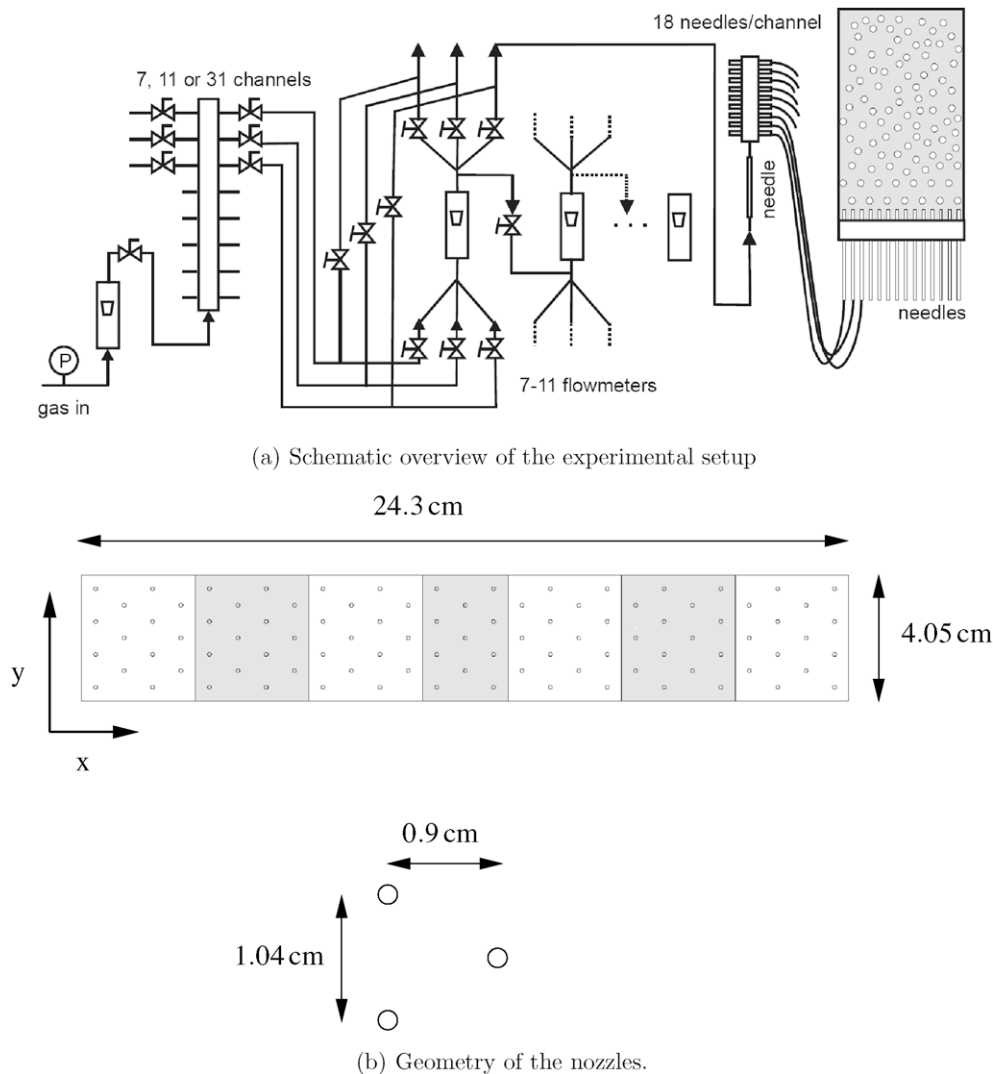

(a) Schematic overview of the experimental setup

(b) Geometry of the nozzles.

Fig. 1. Experimental setup used by Harteveld et al. (2004).

Table 1
Gas injection patterns for use in the pseudo-2D column.

Pattern	Description gas injection	Needles used	Relative area aerated zone (%)	Aeration for
E1	Uniform	95	100	$0 \leqslant x/W \leqslant 1.00$
E2	Central, 1 wall row off	87	93	$0.035 \leqslant x/W \leqslant 0.965$
E3	Central, 2 wall row off	81	85	$0.075 \leqslant x/W \leqslant 0.925$
E4	Central, 3 wall row off	73	78	$0.11 \leqslant x/W \leqslant 0.89$
E5	Central, 4 wall row off	67	70	$0.15 \leqslant x/W \leqslant 0.85$
E6	Asymmetric, 4 wall rows off	81	85	$x/W \leqslant 0.85$
E7	Wall, 3 central rows off	84	89	$x/W < 0.445$ & $x/W > 0.555$

the needles of 0.9 cm in the *x*-direction and 1.04 cm in the *y*-direction, as shown in Fig. 1(b).

The nozzles are arranged in seven groups: one central group of 11 needles and six groups of 14 needles. The ungassed liquid height was 0.70 m. The gas injection pattern was varied to study its influence on the hydrodynamics and flow structures. In total seven injection patterns were investigated by Harteveld et al. (2004), which we refer to as cases E1–E7. The superficial velocity of 0.020 m/s was kept constant when the injection pattern was altered. The patterns are described in Table 1 and schematically depicted in Fig. 2.

2.2. Instantaneous gas and liquid velocity

The large scale structures in the pseudo-2D column were studied with the aid of Particle Image Velocimetry (PIV) and Particle Tracking Velocimetry (PTV). A CCD camera (Dalsa Inc.) with a maximal resolution of 512×512 pix was used to record images of the flow. The lower area ($0<z<0.7$ m) of the column was recorded in two steps, each step imaging an area of 0.24×0.35 m, providing a resolution of 0.64 mm/pix. Both the PIV and PTV analyses were performed with the use of DaVis PIV software from LaVision.

Sequences of images of the bubble motion were recorded and PIV was used to determine the bubble velocities from these sequences. To obtain bubble shadows over a large area of the column is illuminated from the back. This leads to bubble velocities averaged in the depth direction of the column. Fifty pairs of bubble images were captured with a frame rate of 150 Hz. The images were processed using interrogation areas of 32×32 pix with an overlap of 50%. The fifty subsequent velocity fields were then time-averaged to yield a quasi-instantaneous velocity field corresponding to a period of 0.33 s.

The liquid flow was determined by putting tracers in the liquid. Relatively large particles were selected to provide sufficient contrast: polystyrene particles with a diameter of approximately 2.5 mm. Due to the large inertia of the particles, only the largest structures were determined. For the PTV analysis, the images were recorded at a frame rate of 30 Hz over a period of 0.6 s. Due to the presence of the bubbles, most tracer particles were only visible for short periods while some particles were visible for a longer period resulting in a wide variation of vector density. Since the particles were not neutrally buoyant (i.e. having a slip velocity of 0.09 m/s), the results cannot be directly compared with the simulations, but should rather be used to obtain a qualitative impression of the large flow structures.

The PIV and PTV results were obtained from sets of experiments performed on different days, therefore the vector fields do not correspond to the same time instants and the large scale instantaneous structures are different.

2.3. Time-averaged liquid velocity

The average liquid velocity was measured by means of Laser Doppler Anemometry (LDA). For the LDA measurements, the flow was seeded with hollow glass particles, which were neutrally buoyant and were 10 μm in diameter. The equipment consisted of a 4 W Spectra-Physics Ar^+ laser and a TSI 9201 colorburst multicolor beam separator. Beam pairs were focused using a backscatter probe with a lens of 0.122 m focal length. Detected light was sent to the TSI 9230 colorlink. The axial component was determined with green ($\lambda = 514.5$ μm) beams, the tangential

(a) Case E1 (b) Case E2

(c) Case E3 (d) Case E4

(e) Case E5 (f) Case E6

(g) Case E7
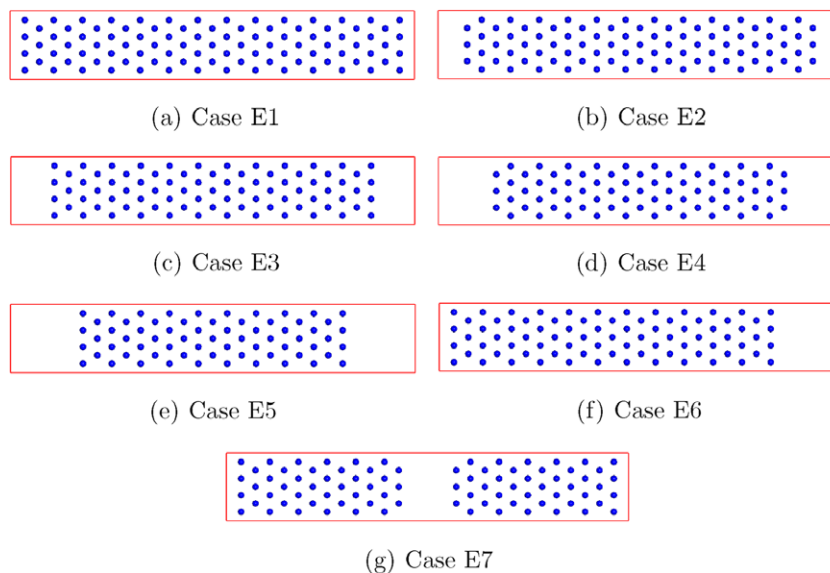
Fig. 2. Gas injection patterns for pseudo-2D column.

component using blue ($\lambda = 488\,\mu$m) beams. The fringe spacings were 1.28 μm (green channel) and 1.22 μm (blue channel). A pre-shift frequency of 500 kHz was used. Bursts were processed with the IFA-750 (TSI) processor. For each measurement point, a time series of 300 s was used.

2.4. Time averaged void fraction

The integral gas hold-up, (ε_I), was determined from the hydrostatic pressure difference over the column.

The spatial distribution of the average gas hold-up is measured by using glass fiber probes (Cartellier, 1992; Mudde and Saito, 2001; Julia et al., 2005). Light is emitted into one end of a glass fiber while the other end is put inside the bubble column facing downward. If the 200 μm diameter tip is located in the water phase, most of the light exits the tip of the probe. If the tip is located in the gas phase, most of the light is reflected backwards. The amount of reflected light is recorded and the relative occurrence of the phases is determined from this signal, which is done via direct sampling of the signal and offline software processing. Five fiber probes are used simultaneously to measure the void fraction over a line from the center of the column to the wall.

The technique generally underestimates the void fraction for the present experimental condition by 10–20%, depending on the type of signal processing that is used. The inaccuracy is corrected by applying the so-called low level criterion and further improved by applying a correction factor which is determined by comparing the results from the glass fiber probes and the integral gas hold-up measurements (see Julia et al. (2005), Harteveld et al. (2004) for further details). The time series in the experiments for the probes had a length of 1000 s. During this time, typically some 15,000 bubbles were collected per probe ($\varepsilon_I \approx 20\%$).

3. Discrete bubble model

A parallel version of the three-dimensional discrete bubble model (DBM) developed by Darmana et al. (2006) is used to model the pseudo-2D bubble column. The liquid phase hydrodynamics is represented by the volume-averaged Navier–Stokes equations while the motion of each individual bubble is tracked in a Lagrangian fashion.

3.1. Bubble dynamics

The motion of each individual bubble is computed from the bubble mass and momentum equations while accounting for bubble–bubble and bubble–wall interactions via an encounter model similar in spirit to the model of Hoomans et al. (1996), using ideal collision properties. The liquid phase contributions are taken into account by the net force $\sum \mathbf{F}$ experienced by each individual bubble. For an incompressible bubble, the equations can be written as:

$$\rho_b V_b \frac{d\mathbf{v}}{dt} = \sum \mathbf{F} \tag{1}$$

where ρ_b, V_b and $\mathbf{v}$ respectively represent the density, volume and velocity of the bubble. The net force acting on each individual bubble is calculated by considering all the relevant forces. It is composed of separate, uncoupled contributions which in the present study include: gravity, far field pressure, drag, lift, virtual mass and wall forces:

$$\sum \mathbf{F} = \mathbf{F}_G + \mathbf{F}_P + \mathbf{F}_D + \mathbf{F}_L + \mathbf{F}_{VM} + \mathbf{F}_W \tag{2}$$

Expressions for each of these forces used in the present study can be found in Table 2. Note that the drag, lift and wall force closures used in the present study are obtained from Tomiyama et al. (2002), Tomiyama et al. (1995). In the current work we assume there is no bubble coalescence and breakup, which is a faire assumption, given the fact that no large bubbles were observed in the experiments. Furthermore, bubble induced turbulence or void fraction corrections on the interfacial forces are not considered here.

3.2. Liquid phase hydrodynamics

The liquid phase hydrodynamics are represented by the volume-averaged Navier–Stokes-equations, which consist of the continuity and momentum equations. The presence of bubbles is reflected by the liquid phase volume fraction ε_ℓ and the interphase momentum transfer Φ:

$$\frac{\partial}{\partial t}(\varepsilon_\ell \rho_\ell) + \nabla \cdot \varepsilon_\ell \rho_\ell \mathbf{u} = 0 \tag{3}$$

$$\frac{\partial}{\partial t}(\varepsilon_\ell \rho_\ell \mathbf{u}) + \nabla \cdot \varepsilon_\ell \rho_\ell \mathbf{u}\mathbf{u} = -\varepsilon_\ell \nabla P - \nabla \cdot \varepsilon_\ell \tau_\ell + \varepsilon_\ell \rho_\ell \mathbf{g} + \Phi \tag{4}$$

where $\mathbf{g}$ is the gravity constant, ρ_ℓ, $\mathbf{u}$ and P respectively the density, velocity and pressure for the liquid phase.

Table 2
Overview of forces acting on a bubble.

Force	Closure
$\mathbf{F}_G = \rho_b V_b \mathbf{g}$	–
$\mathbf{F}_P = -V_b \nabla P$	–
$\mathbf{F}_D = -\frac{1}{2} C_D \rho_l \pi R_b^2 \|\mathbf{v} - \mathbf{u}\|(\mathbf{v} - \mathbf{u})$	$C_D = \max[\min\left[\frac{16}{Re}(1 + 0.15Re^{0.687}), \frac{48}{Re}\right], \frac{8}{3}\frac{E\ddot{o}}{E\ddot{o}+4}]$
	$Re = \frac{\rho_\ell(\mathbf{u}-\mathbf{v})d_b}{\mu_{L\ell}}$
	$E\ddot{o} = \frac{g\Delta\rho d_b^2}{\sigma}$
$F_L = -C_L \rho_\ell V_b (\mathbf{v} - \mathbf{u}) \times \nabla \times \mathbf{u}$	$C_L = \begin{cases} \min[0.288\tanh(0.121Re), f(E\ddot{o}_d)]; E\ddot{o}_d < 4 \\ f(E\ddot{o}_d); 4 < E\ddot{o}_d \leqslant 10 \\ -0.29; E\ddot{o}_d > 10 \end{cases}$
	$f(E\ddot{o}_d) = 0.00105E\ddot{o}_d^3 - 0.0159E\ddot{o}_d^2 - 0.0204E\ddot{o}_d + 0.474$
	$E\ddot{o}_d = \frac{E\ddot{o}}{E^{2/3}}; E = \frac{1}{1+0.163E\ddot{o}^{0.757}}$
$\mathbf{F}_{VM} = -C_{VM}\rho_\ell V_b\left(\frac{D_b\mathbf{v}}{D_b t} - \frac{D_l\mathbf{u}}{D_l t}\right)$	$C_{VM} = 0.5$
$\mathbf{F}_W = C_W R_b \rho_\ell \frac{1}{D_{bw}^2}\|\mathbf{u} - \mathbf{v}\|^2 \cdot \mathbf{n}$	$C_W = \begin{cases} e^{(-0.933Eo+0.179)} & 1 < Eo < 5 \\ 0.0007Eo + 0.04 & Eo \geqslant 5 \end{cases}$

The momentum transfer rate from the bubbles to the liquid, Φ, is calculated as:

$$\Phi = \frac{1}{V_{\text{cell}}} \sum_{i=1}^{N_b} \phi D(\mathbf{x} - \mathbf{x}_i) \tag{5}$$

where ϕ is the reaction of the momentum transfer exerted on the bubbles, $\phi = -\sum \mathbf{F}$ and D is an approximate Delta function to map the force from the Lagrangian position of bubble i, $\mathbf{x}_i$ to the Eulerian position in the grid, $\mathbf{x}$. In this work, a clipped fourth-order polynomials function is used following the work of Deen et al. (2004). In addition a similar mapping technique is used to map the bubble volume for the calculation of the gas volume fraction (see (Darmana et al., 2006) for more detail concerning the mapping technique).

Both phases are assumed to be incompressible, which is a reasonable assumption considering the limited height of the simulated systems. The liquid phase stress tensor τ_ℓ is assumed to obey the general Newtonian form given by:

$$\tau_\ell = -\mu_{\text{eff},\ell} \left[((\nabla \mathbf{u}) + (\nabla \mathbf{u})^T) - \frac{2}{3}\mathbf{I}(\nabla \cdot \mathbf{u}) \right] \tag{6}$$

where $\mu_{\text{eff},\ell}$ is the effective viscosity. In the present model the effective viscosity is composed of two contributions, the molecular viscosity and the turbulent viscosity:

$$\mu_{\text{eff},\ell} = \mu_{\text{L},\ell} + \mu_{\text{T},\ell} \tag{7}$$

where the turbulent viscosity $\mu_{\text{T},\ell}$ is calculated using the sub-grid scale (SGS) model of Vreman (2004):

$$\mu_{\text{T},\ell} = 2.5 \rho_\ell C_S^2 \sqrt{\frac{B_\beta}{\alpha_{ij}\alpha_{ij}}} \tag{8}$$

where C_s is a model constant for which a typical value of 0.1 was used, $\alpha_{ij} = \partial u_j / \partial x_i$, $\beta_{ij} = \Delta_m^2 \alpha_{mi}\alpha_{mj}$ and $B_\beta = \beta_{11}\beta_{22} - \beta_{12}^2 + \beta_{11}\beta_{33} - \beta_{13}^2 + \beta_{22}\beta_{33} - \beta_{23}^2$. Δ_i is the filter width in the i direction, which is equal to the computational grid size in the respective direction. It is noted here that this SGS model was constructed in such a way that its dissipation is relatively small in transitional and near-wall regions, which therefore does not require any wall damping.

In the Lagrangian description of the bubbles, it is assumed that the interfacial forces can be decoupled and closed with suitable interfacial force closures. It is inherent to this approach to use a computational grid that is of the same scale or larger than the scale of the bubbles. This introduces a somewhat awkward situation: to resolve all details up to the inertial subrange as one would do in a true LES of single phase flows, one would require a grid size of $O(1 \text{ mm})$, whereas for a sensible Lagrangian description of the bubble behavior one would require a grid of $O(1 \text{ cm})$. The choice in this work is a compromise, i.e. the grid spacing is 2.5 mm (the bubble size is 4 mm). Investing additional grid resolution to resolve the boundary layers in more detail will not improve the physical description of the bubbles. In fact, since the bubbles are driving the flow, their description largely determines the quality of the prediction. It is important to realize that the SGS model in this work is merely an estimate of the unresolved sub-grid scale stresses. In the simulations typically dimensionless wall spacing values of $y+ = 15$ are used. Hence, the simulation results in this work should not be viewed as large eddy simulations.

The numerical solution of the liquid phase conservation equations is based on the SIMPLE algorithm Patankar and Spalding (1972) and applied to solve the volume averaged Navier–Stokes equation. The computational cells are labeled by indices (i,j,k) which are located at the cell center and a staggered grid is employed to prevent numerical instability. Using this arrangement the scalar variables are defined at the cell centres whereas the velocities are defined at the cell faces.

First-order time differencing is applied, whereas for the discretization of mass and momentum convection terms, the second order accurate Barton scheme of Centrella and Wilson (1984) is used. In the discretization of the momentum equation the terms associated with the continuous phase pressure gradients are treated fully implicitly while the interphase momentum transfer and other terms are treated explicitly.

4. Simulations

All of the experimental cases E1–E7 explained in Section 2 are modeled using the three dimensional DBM which we refer to as cases S1–S7 respectively. The applied computational grid consists of $101 \times 17 \times 290$ uniform cells and the time step, δt_{flow} is set to 1×10^{-3} s while for the bubble tracking (δt_{bub}) a time step of 1×10^{-4} s is used. Note that the bubble response time for a 4 mm bubble is about 1×10^{-3} s. Earlier calculations revealed that this configuration gives a grid and time step independent solution (van den Hengel et al., 2005). Note that the grid used in this work is twice as fine as the finest grid used in the work of van den Hengel et al. (2005), so grid independence can be assumed.

The boundary conditions are imposed to the column using the flag matrix concept of Kuipers et al. (1993) as is shown in Fig. 3. The definition of each boundary condition can be found in Table 3.

Each nozzle in the experimental setup is modeled as a position in the bottom of the column where bubbles with specific size enter the column with a fixed velocity. All the bubbles entering the column have a diameter of 4 mm (Harteveld et al., 2004 observed that the inlet bubbles may vary from 3.5 to 4.5 mm). The distance between the center of two consecutive bubbles released from a single hole δ_b is set to $2.5 \times R_b$. This arrangement is made to avoid unnecessary collisions between two consecutive bubbles immediately after they enter the column. The velocity of bubbles entering the column is determined from the superficial velocity through the following formula:

$$v_{z,\text{enter}} = \frac{v_s \delta_b W \times D}{N_h V_b} \tag{9}$$

with v_s the superficial gas velocity, $W \times D$ the cross sectional area of the column and N_h is number of holes.

For all of the nozzles, the vertical position of the bubbles underneath the bottom plate is generated in such way that none of the bubbles enter the column at the same time. This was implemented in order to prevent (artificial) pulsing behavior of the incoming bubbles, which would occur if bubbles enter the column through
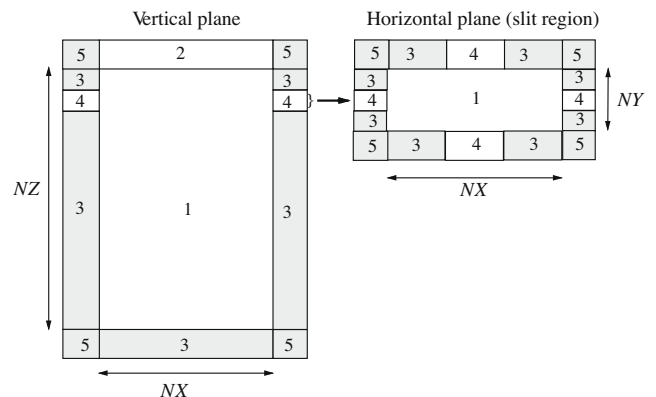

Fig. 3. Typical boundary conditions used in simulations with the discrete bubble model. The vertical plane is at $j = NY/2$ while a slit is defined at $k = NZ - 1$.

Table 3
Cell flags and corresponding cell types used in defining boundary conditions.

Flag	Boundary conditions
1	Interior cell, no boundary conditions specified
2	Impermeable wall, free slip boundary
3	Impermeable wall, no slip boundary
4	Prescribed pressure cell, free slip boundary
5	Corner cell, no boundary conditions specified

all holes simultaneously. By doing so, the occurrence of undesired pressure fluctuations at the top of the column was prevented.

During the simulation on average about 19,000 computational bubbles are present in the calculation. This amount of bubbles is resulting from the balance between bubbles coming into the column through the nozzle and the bubbles leaving the column from the top surface. For every simulated second, it takes about 24 h calculation time using 8 processors on a SGI Altix 3700 system with Intel Itanium 2, 1.3 GHz processors.

5. Result and discussion

In this section the results obtained from the DBM model will be presented and compared with experimental data. First, the flow structures during the startup period resulting from simulation will be shown. Then, the flow structures present after the flow has fully developed will be compared with experimental observations. Finally, the comparison between simulation results and experimental data on the bases of averaged quantities will be addressed.
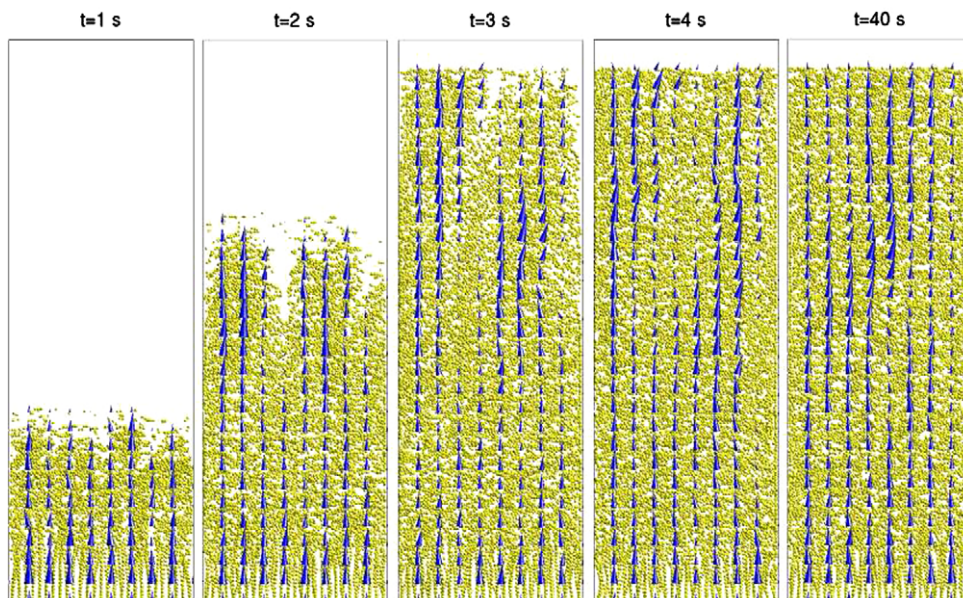
5.1. Flow structures during the startup period

All simulations were carried out by injecting bubbles into an initially quiescent liquid. Depending on the injection pattern, bubbles will rise through the liquid and occupy the column space with different patterns until a fully developed condition is reached. Fig. 4 shows series of snapshots of the bubble structures during the startup period resulting from the DBM simulation for case S1 (fully aerated column). As can be seen, the bubbles are rising in a uniform fashion and filling the entire column in the lateral direc-

tion right from the start. In a later stage some bubbles are rising faster than others and split the bubble population into two groups. This situation however does not sustain for a long time as the bubbles in the lower part of the column still move in a homogeneous fashion. At about t = 3 s some bubbles start to leave the top surface and the column starts to exhibit a uniform flow pattern where bubbles are present everywhere and rising with relatively uniform velocity.

The results from the partially aerated cases (i.e. cases S2–S5) can be seen in Figs. 5 and 6. Here, the non-aerated regions are introduced starting from the wall regions and continually increasing toward the center region of the column. As can be seen, by introducing non-aerated regions, vortices start to develop on both sides of the bottom corner. The two vortices push the bubbles toward the center region creating a necking zone that expands as the non-aerated zone increases. Outside the necking zone, the bubbles are pushed back toward the left and right wall filling up the entire column in the lateral direction. In the upper part of the flow, a typical mushroom shaped structure is found. The roof of the mushroom shape is relatively flat in case S2 and is gradually transformed showing a more sharp roof as the non-aerated zone is increased.

After the bubbles start to leave the top surface, the bubble pattern in cases S2 and S3 show a stable structure where all bubbles are uniformly distributed through out the entire column and uniformly move in the vertical direction (except for the bottom corner regions). In cases S4 and S5 however, the bubbles behave differently. Here, bubbles are moving upward as a meandering plume in the center region of the column. The two vortices in the inlet region have become bigger and stronger. These vortices are strong enough to trap and drag along large portions of the bubbles for some times until they finally escape and rejoin the bubbles in the plume region. After a while however these structures are less pronounced; nevertheless the large circulation cells are still noticeable.

The startup period for the asymmetric injection pattern (case S6) is shown in Fig. 7(top). For case S6 the non-aerated region is only near the right wall, creating vortices in that region. The vortices push the bubbles further toward the left wall generating a larger vortical zone. Higher up in the column the bubbles that were

Fig. 4. Series of instantaneous solution for case S1 during the startup period showing the bubble structures and their velocities.
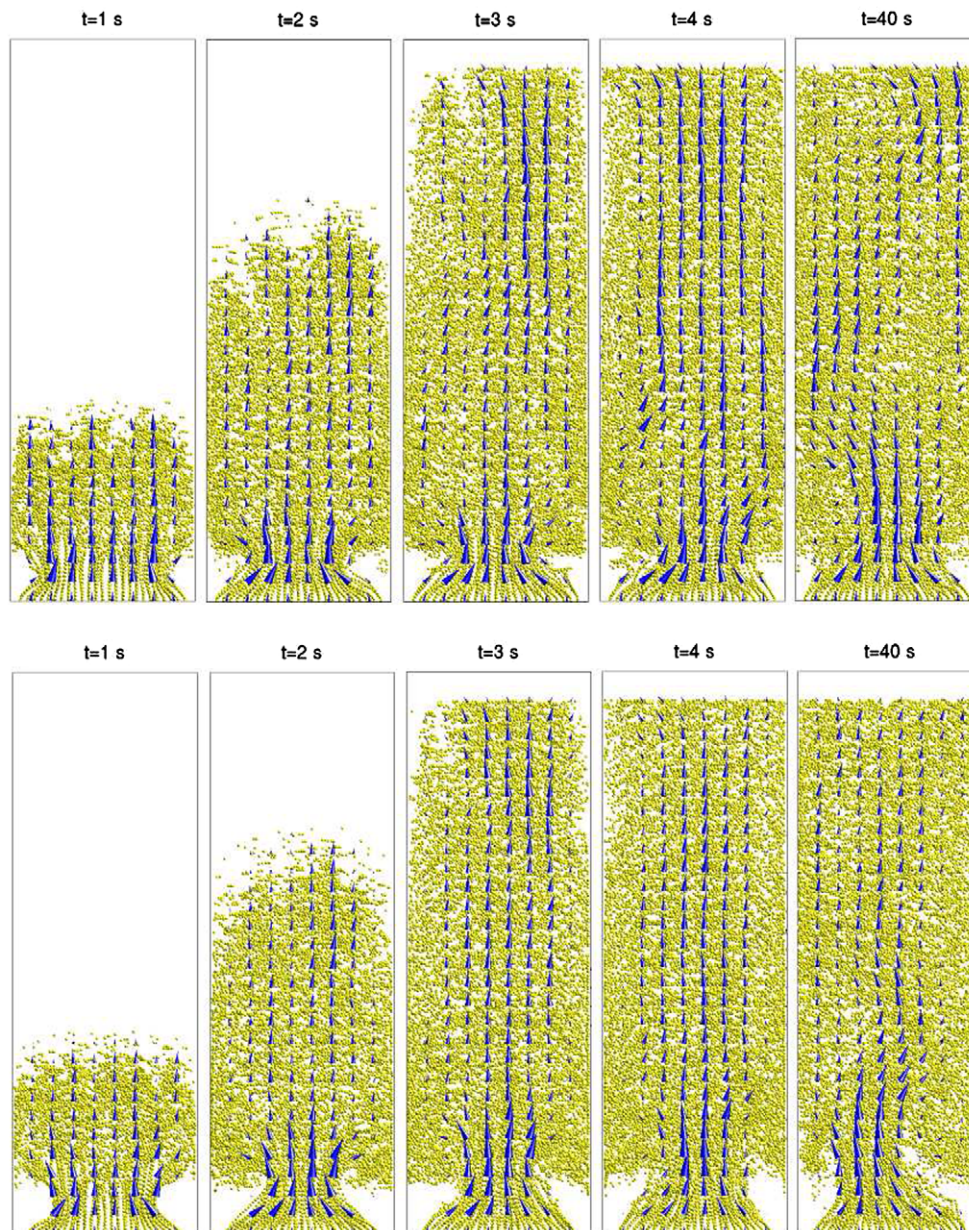
Fig. 5. Instantaneous solution for cases S2 (top row) and S3 (bottom row) during the startup period.

pushed aside by the vortices are moving back toward the right wall filling the column in the lateral direction. Later on, the same vortices trap large portions of bubbles and drag them down filling up the gap in the right corner. The top region of the structures is similar with half of the structures found on the partially aerated bubble columns (cases S2–S5), showing a mushroom shaped structure which moves in the vertical direction and later on fills up the entire column except the area close to the non-aerated inlet.

The flow structures appearing during the startup in the case that the center region is non-aerated (case S7) is shown in Fig. 7 (bottom). In this case, the bubbles initially rise in two groups separated by the non-aerated zone. At about $z > 10$ cm the two groups rejoin, generating a liquid area enclosed by bubbles. At a higher position, the bubbles are again splitted into two groups as they ascend to the liquid surface. The two groups of bubbles are not present for long time and disappear after about $t = 4$ s. Afterwards, the bubbles fill the entire top region of the column uniformly, while the void region close to the non-aerated area starts to meander irregularly from left to right.

5.2. Fully developed flow structures

Comparison between simulation results and experimental observations after the flow has fully developed can be seen in Figs. 8–14. Here the bubble velocity resulting from the DBM simulations is averaged in the depth direction to mimic the bubble velocity resulting from the PIV measurements, while the liquid velocity in a slice positioned at $y/D = 0.5$ is presented. The figures indicate that the flow structures found in the experiments and simulations are similar to a large degree. For uniform gas injection the patterns found in the experiment (case E1) and simulation (case S1) show a perfect resemblance (see Fig. 8). In both cases the bubbles are distributed uniformly over the entire region of the column. Furthermore, for both cases a rectilinear bubble path can be observed close to the inlet area before the interaction between bubbles and the liquid makes the bubble paths more irregular. The close resemblance can also be observed in the bubble velocity; i.e. the bubbles show a similar tendency to rise with more or less uniform velocity. In the liquid velocity no large structures are observed for
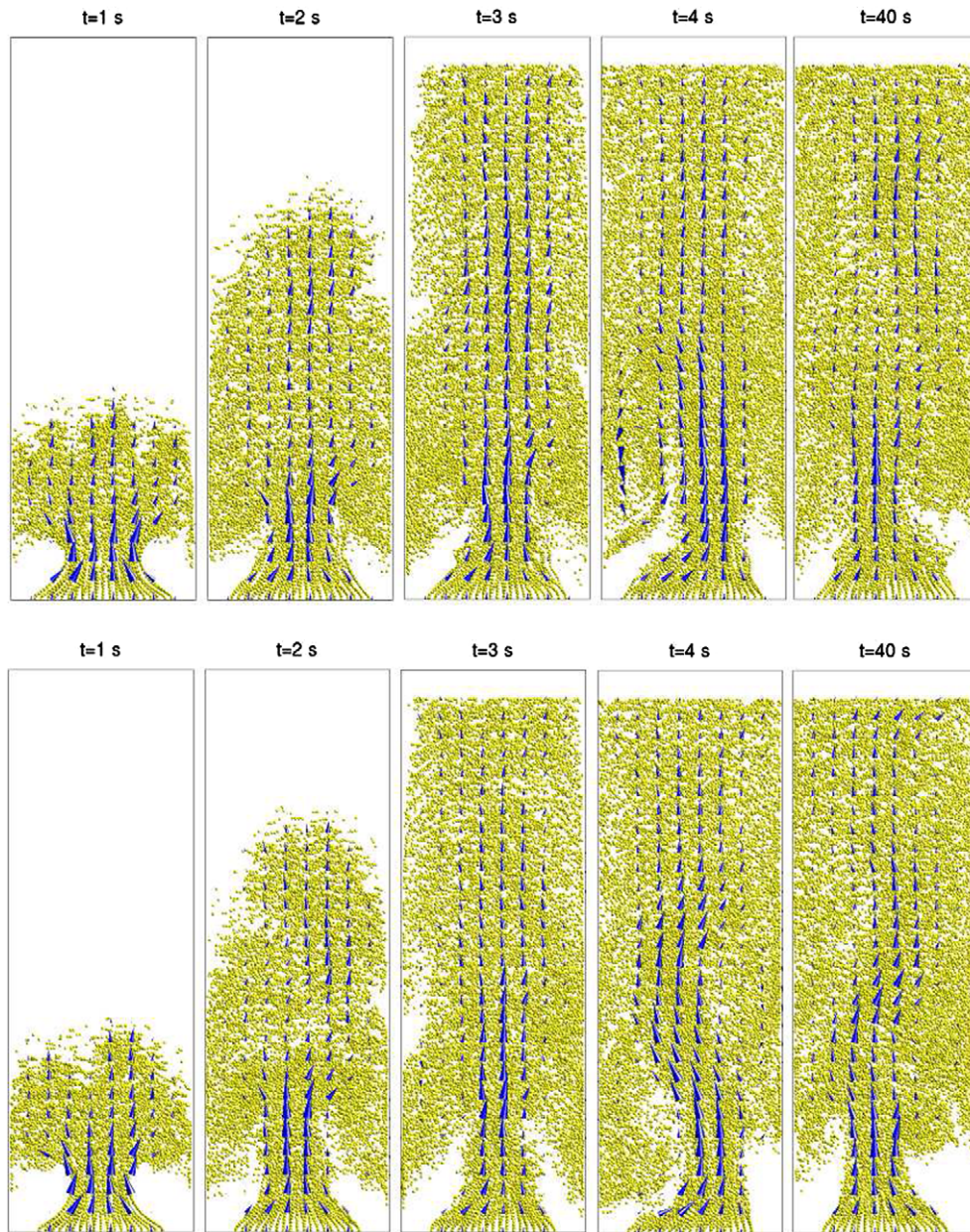
Fig. 6. Instantaneous solution for cases S4 (top row) and S5 (bottom row) during the startup period.

both cases, which further confirms the uniformity of the flow field. When small non-aerated regions are introduced in both lower corners of the column, a small discrepancy between experimental observation (case E2) and the simulation result (case S2) appears (see Fig. 9). In this case, vortices are present in both corners; however, the vortices predicted by the simulation are bigger in size than in the experimental counterpart. In the simulation, the bubble paths are more converged immediately after injection to the column, resulting in a tighter necking zone compared with the experiment. Consequently, the size of the flow development region is over-predicted. The bubble velocity field resulting from case S2 shows that the bubbles are accelerated in the necking zone, while the velocity in the circulation zone is very low. This situation is not observed in case E2. In the top of the column, similar structures are obtained for both cases where bubbles rise uniformly toward the column surface. The differences are probably due to the fact that the DBM does not fully resolve the flow around the bubbles, leading to different flow fields especially for bubbles that only have

neighboring bubbles on one side, i.e. on the edge of a bubble plume.

As the non-aerated zone is increased from 7% to 15%, the vortices near both corners of the inlet region are growing, as is shown in Fig. 10. Here, the experimental result (case E3) shows a pronounced vortical zone on both sides of the inlet resulting in a necking zone. Comparing with case S3 however, these vortices are smaller and the necking zone is bigger. The upper part of the column shows relatively similar structures, where bubbles distribute almost uniformly in the lateral direction. The accelerated bubbles in the necking zone are now subsequently propagated to the surface of the column generating a snake-like bubble plume, where bubbles move faster compared to the bubbles outside the plume. This structure is observed in both experiment and simulation, which is also resembled in the liquid velocity field, where multiple circulation cells are stacked in the axial direction. A similar situation is also found when the non-aerated zone is further increased from 15% to 22%, as is shown in Fig. 11.
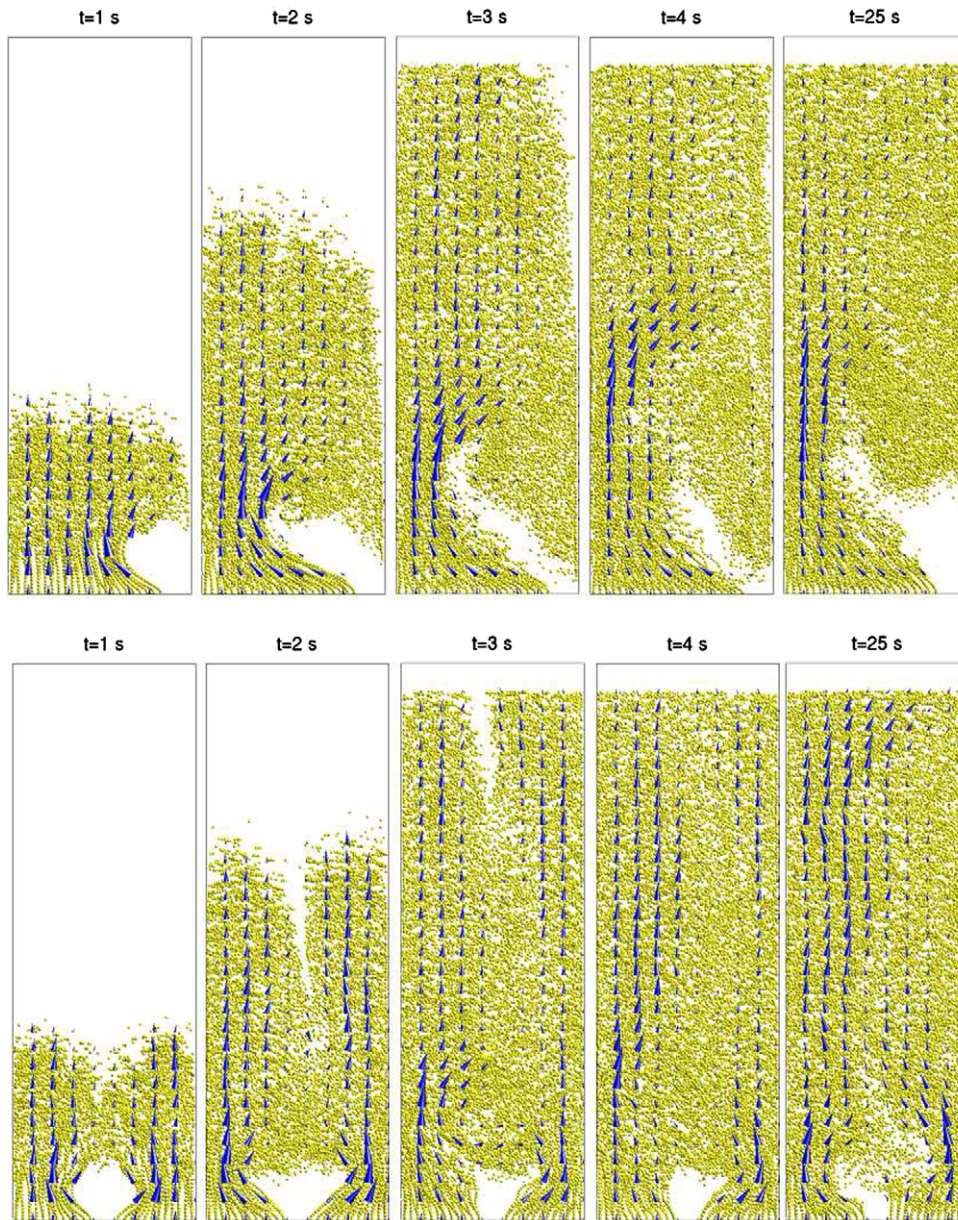
Fig. 7. Instantaneous solution for cases S6 (top row) and S7 (bottom row) during the startup period.

Fig. 12 shows that expanding the non-aerated zone from 22% to 30% results in a different flow pattern. Here, the simulation result (case S5) shows a pronounced bubble plume structure, where "piles of bubbles" are packed together starting from the inlet up to the column surface. Some of the bubbles are trapped in a circulation zone, which is strong enough to drag the bubbles down and fill up the region outside the bubble plume. This structure however is less pronounced in the experiment (case E5). Furthermore, a high bubble velocity in the bubble plume can be observed for both cases E5 and S5, which is also reflected in the liquid velocity field.

In the case of the non-aerated zone on one side of the column (i.e. cases E6/S6) the comparison between the simulation and the experiment shows good resemblance (see Fig. 13). Both cases show that the bubbles are pushed toward the left wall by the strong vortices, while some of the bubbles are dragged down by the same vortices. In the top region, bubbles fill the entire region of the column, however in case E6 the effect of the circulation pattern to the bubble structure is more pronounced compared to the

experimental counterpart. The bubble velocity also shows good similarity between the two cases, where bubbles moving in the plume have a high upflow velocity, while the bubbles inside the large vortices have a tendency to move along with it. In the liquid velocity field, several (fixed) circulation cells are found, which are stacked in the axial direction. It is noted that the number of circulation cells as well as their size is rightly predicted by the simulations.

Finally for the cases where the gas is injected near the wall but not in the center (cases E7/S7), again we find good resemblance as shown in Fig. 14. For both cases we find some vortical structure in the lower part of the column, which move around quite irregularly. These structures however are not found in the higher regions of the column ($z > 0.2$ m).

5.3. Integral gas hold-up

The comparison of the integral gas hold-up obtained from the simulations and experiments is given in Fig. 15. The total gas
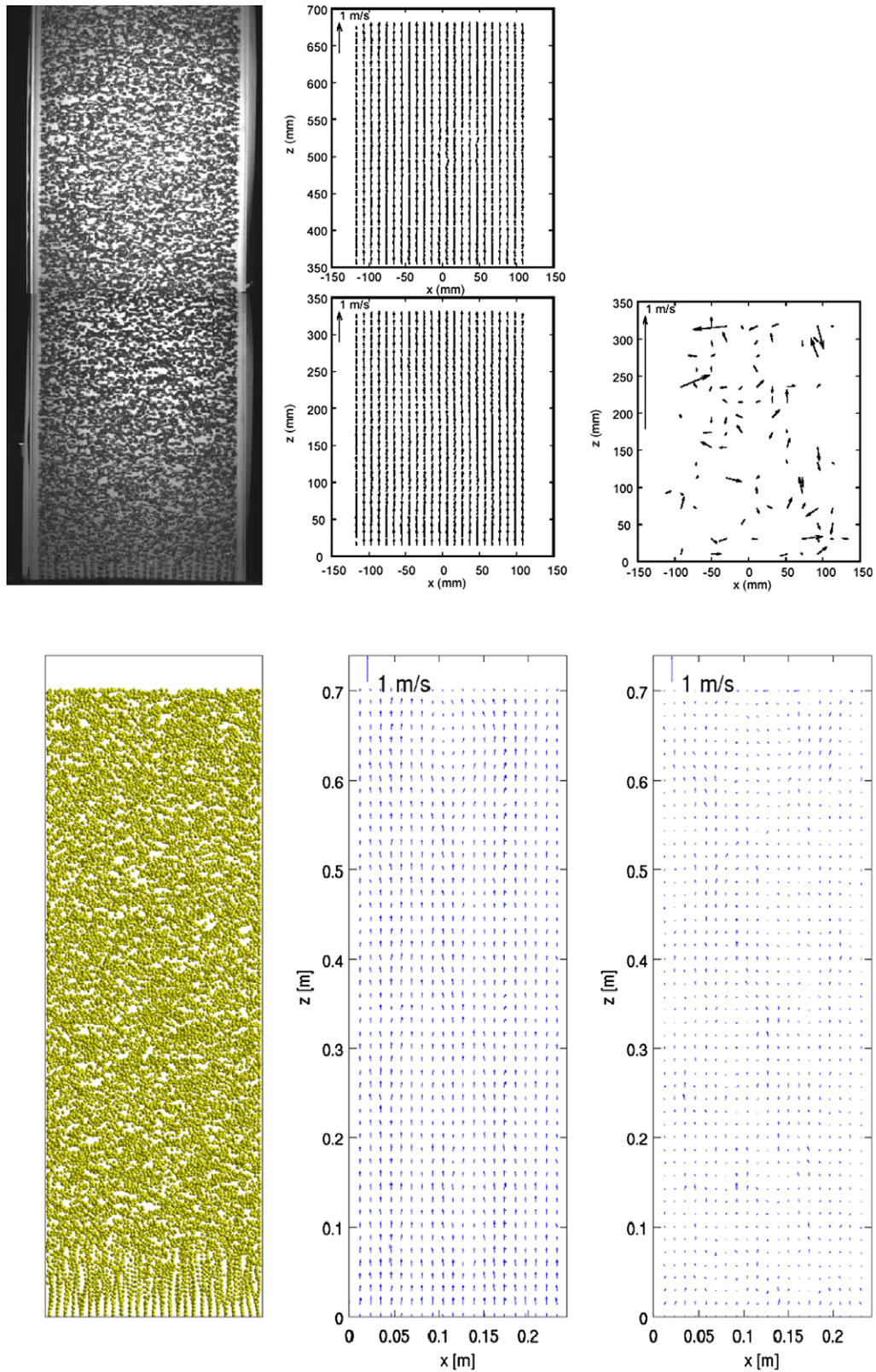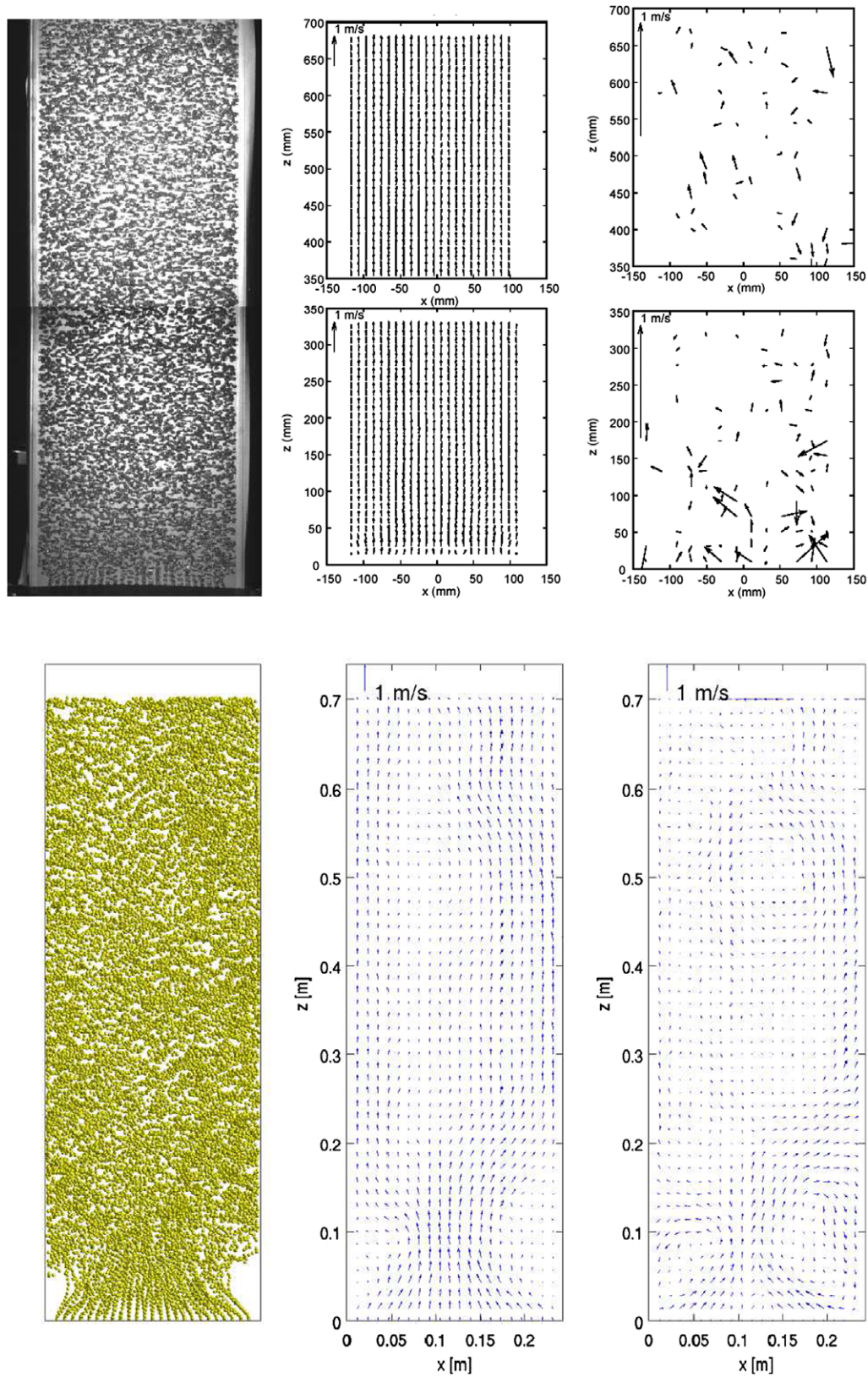
Fig. 8. Instantaneous flow structure comparison between cases E1 (top row) and S1 (bottom row). From left to right: bubble positions, bubble velocity and liquid velocity.

hold-up in the simulations is obtained by calculating the total volume of all bubbles present in the column divided by the total volume of the column while the experimental gas hold-up is ob-tained by measuring the total expansion of the dispersion in the column. The figure shows that the simulation results reflect the same trend as observed in the experiments. By increasing
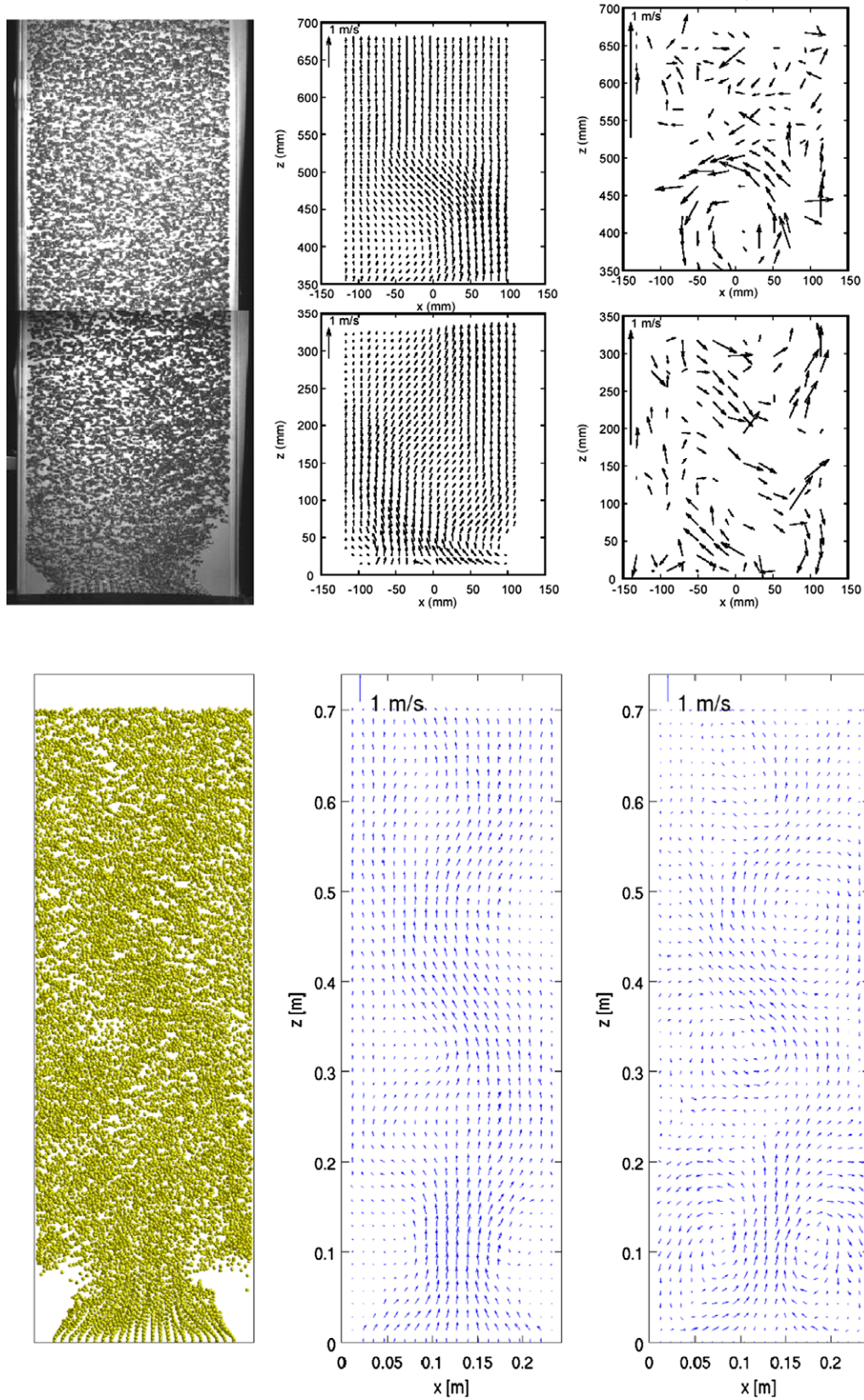
Fig. 9. Instantaneous flow structure comparison between cases E2 (top row) and S2 (bottom row). From left to right: bubble positions, bubble velocity and liquid velocity.

the non-aerated zone in cases 1–5 the integral gas hold-up is consistently decreasing despite the fact that the superficial velocity is kept constant. As the top part of the column is having a relatively similar bubble population, the decrease in the gas hold-up can be attributed to the increasing size of vortices close to the non-aerated region. A similar situation occurs in cases 6 and 7. Quantitative comparison between experiment and simulation however shows that the simulations consistently overpredict
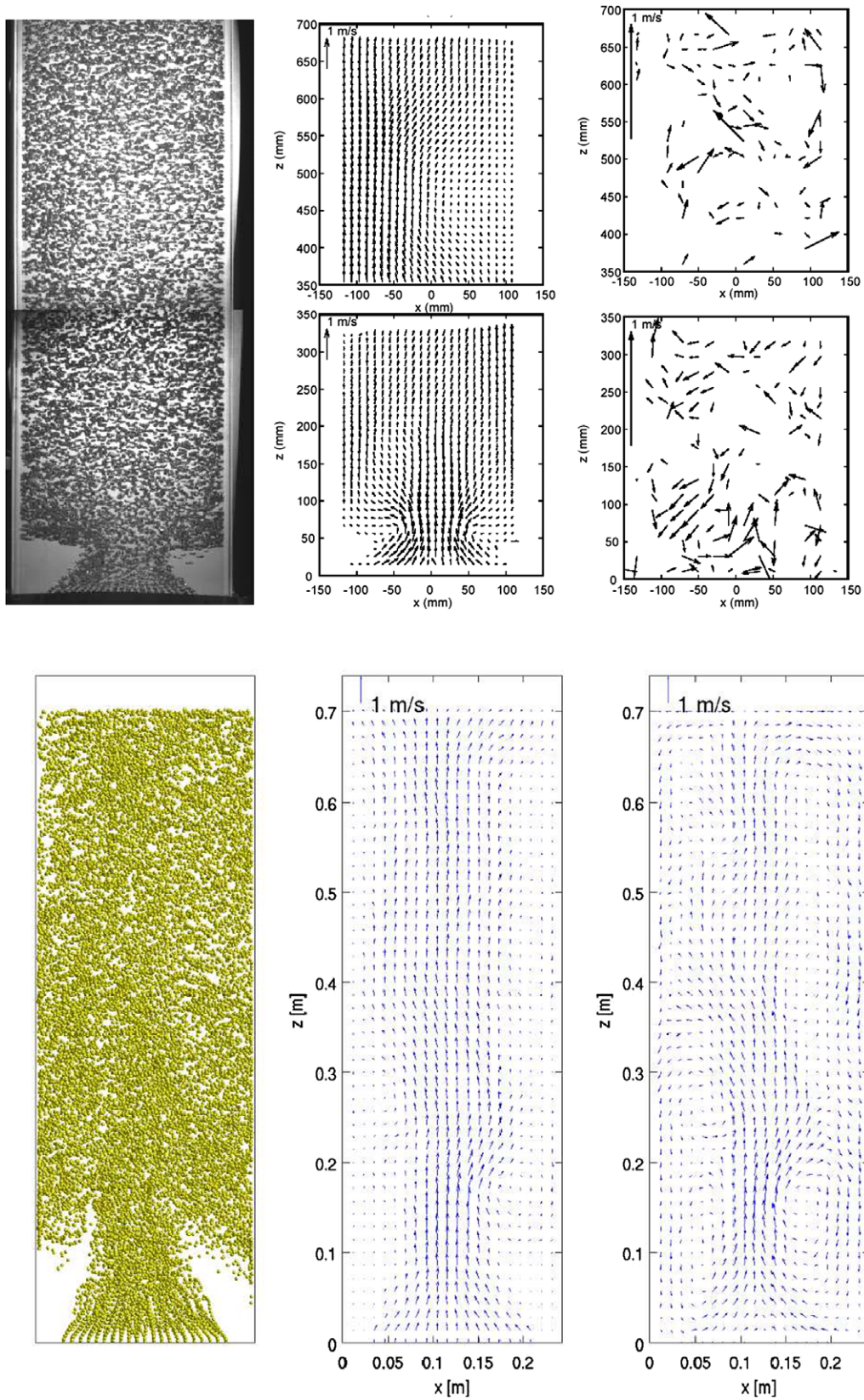
Fig. 10. Instantaneous flow structure comparison between cases E3 (top row) and S3 (bottom row). From left to right: bubble positions, bubble velocity and liquid velocity.

the experimental data with about 25%. This can most probably be related to an underestimation of the terminal bubble velocity, i.e. $v_\infty \approx 0.23$ m/s in the simulations and $v_\infty \approx 0.27$ m/s in the experiments.

5.4. Time-averaged quantities

The time-averaged quantities in the simulations are calculated using the following relation:

Fig. 11. Instantaneous flow structure comparison between cases E4 (top row) and S4 (bottom row). From left to right: bubble positions, bubble velocity and liquid velocity.

$$\bar{\phi} = \frac{1}{N_t} \sum_{i=1}^{N_t} \phi_i \quad (10)$$

where ϕ is the quantity at hand, N_t is the number of time steps used in the averaging. While the RMS value of the quantity is calculated as:
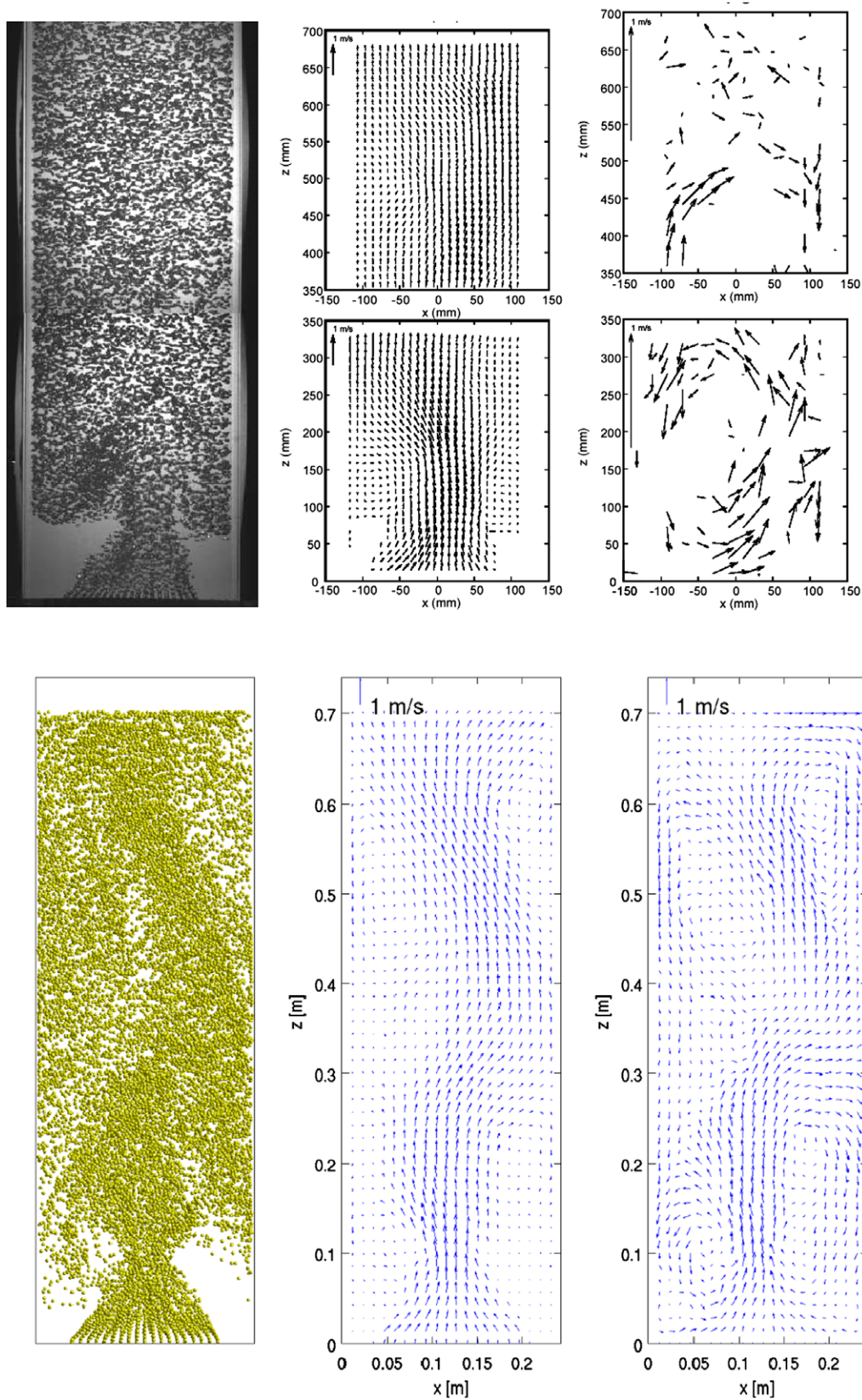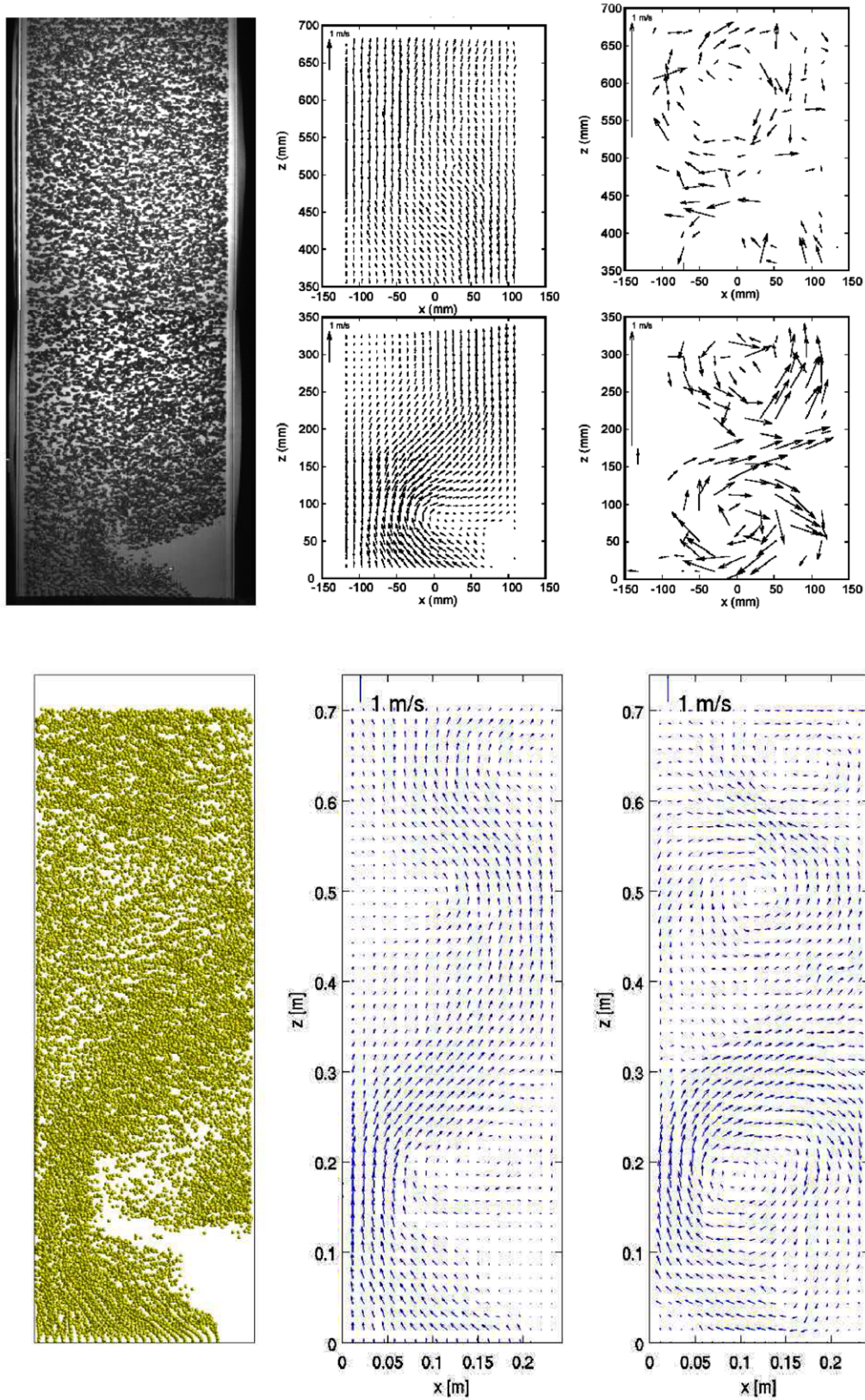
Fig. 12. Instantaneous flow structure comparison between cases E5 (top row) and S5 (bottom row). From left to right: bubble positions, bubble velocity and liquid velocity.

$$\phi' = \frac{1}{N_t}\sqrt{\sum_{i=1}^{N_t}(\phi_i - \bar{\phi})^2} \qquad (11)$$

In the experiments the liquid velocity is measured using the LDA technique as described in Section 2.3. For the uniform gas injection (case 1) the comparison between the experimental and simulation

Fig. 13. Instantaneous flow structure comparison between cases E6 (top row) and S6 (bottom row). From left to right: bubble positions, bubble velocity and liquid velocity.

results can be found in Fig. 16. As can be seen, the velocity profile resulting from the simulation shows similarity with the experimental results where upflow is present in the center region, while downflow is present close to the wall. At a height of $z = 0.05$ m a discrepancy between simulation and experiment exists; here the simulation

shows a core peaking velocity profile, while the experiment shows wall peaking. At first thought this might be attributed to the lift or wall forces, which often are drivers for lateral variations in gas holdup and velocity. However, in this case the gas fraction is distributed homogeneously over the cross section of the column. This makes that
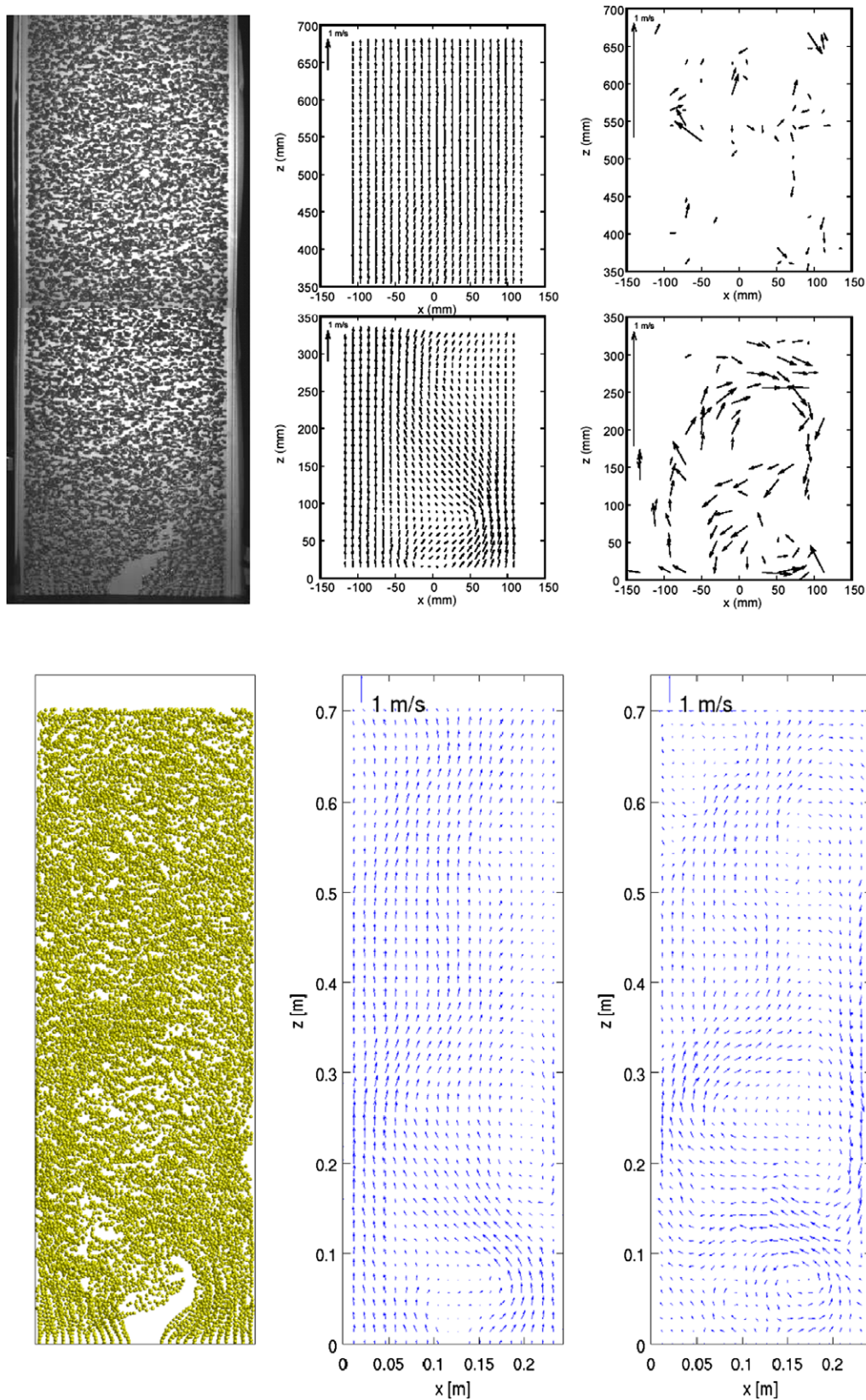
Fig. 14. Instantaneous flow structure comparison between cases E7 (top row) and S7 (bottom row). From left to right: bubble positions, bubble velocity and liquid velocity.

the observed discrepancies cannot be explained through the lift force. The effect of the wall force is seen in the downflow of liquid near the confining walls. However, the effect of wall peaking of the liquid velocity remains unexplained. As the details of the flow around indi-

vidual bubbles are not resolved by the model, it is not possible to use the model to explain this phenomenon.

At higher levels in the column the simulation agrees with the experiment, where the velocity shows upflow in the center of the
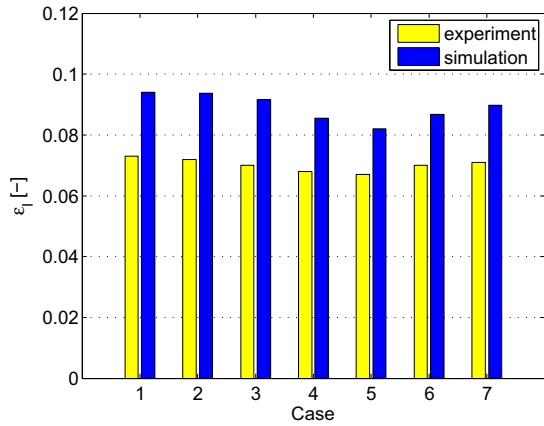
Fig. 15. Integral gas hold-up, comparison between simulation and experiment.

column and downflow close to the walls. Further comparison shows that the velocity profile of the simulation has a higher value in the center compared to the experiment, while close to the wall the downflow predicted by the simulation is also stronger compared to the experiment. A similar situation can be seen in the velocity profile in the depth direction. We suspect that this discrepancy is resulting from the fact that in the experiment liquid is flowing in between bubbles generating a microscale circulation, generating a rather flat velocity profile. Meanwhile in the simulation due to the limitation of the modeling of the bubble dynamics, only the large circulation pattern liquid flow patterns can be resolved. Due to the fact that the flow at the scale of the bubble is not resolved, such effects might only be governed by incorporating a bubble induced turbulence model. The averaged velocity profile in the lower part of the column (i.e. $z = 0.05$ m) for all cases is shown in Fig. 17. From this figure we can see that due to the different injection patterns applied in each case, different velocity
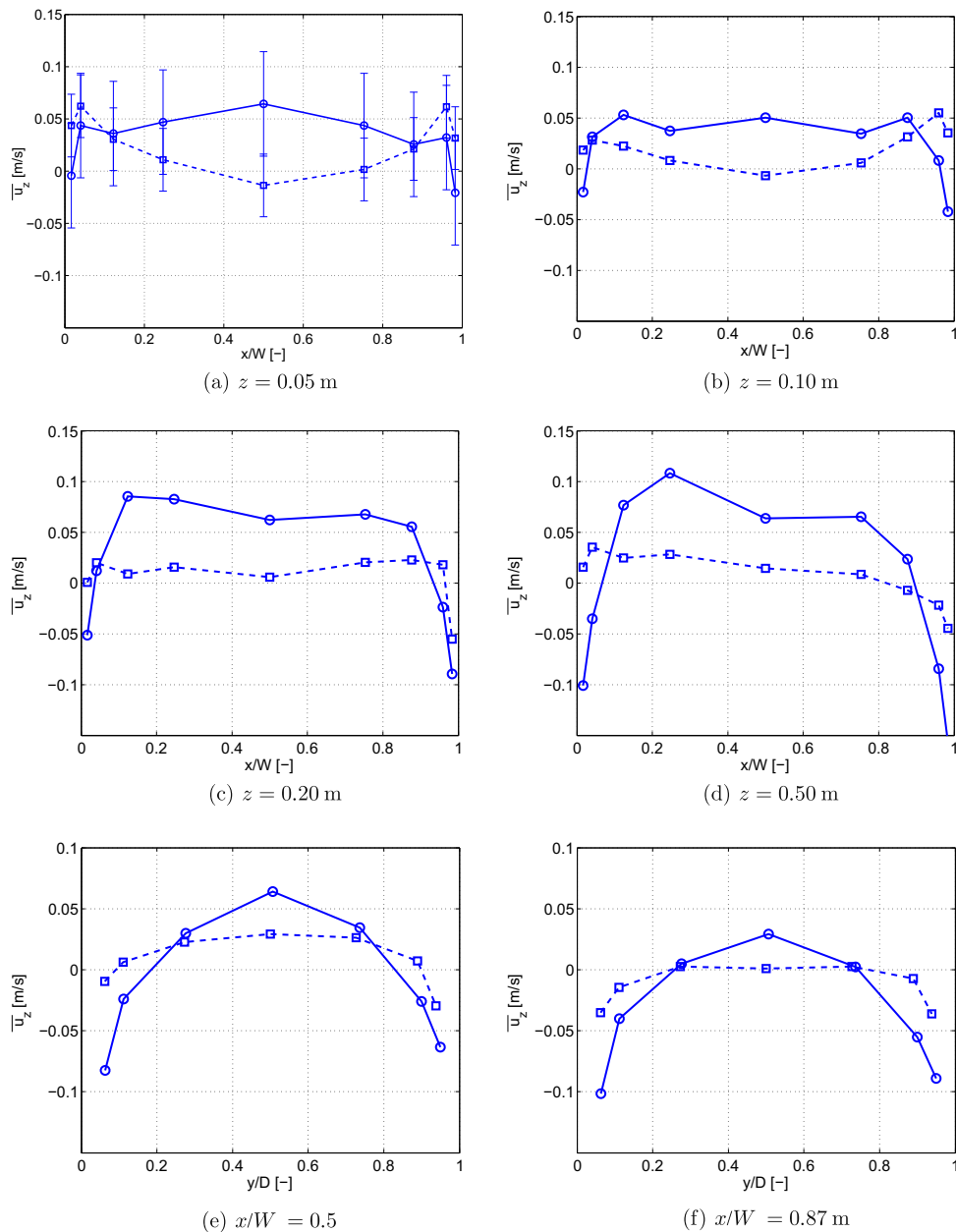

Fig. 16. Velocity profile for uniform gas injection (case 1) at the center line with $y/D = 0.5$ (first two rows) and over two lines in the y-direction ($z = 0.5$ m) (last row). Continuous line: simulation, dashed line: experiment. Error bars are shown for $z = 0.05$ m only. For the other plots the error bars have a similar magnitude.
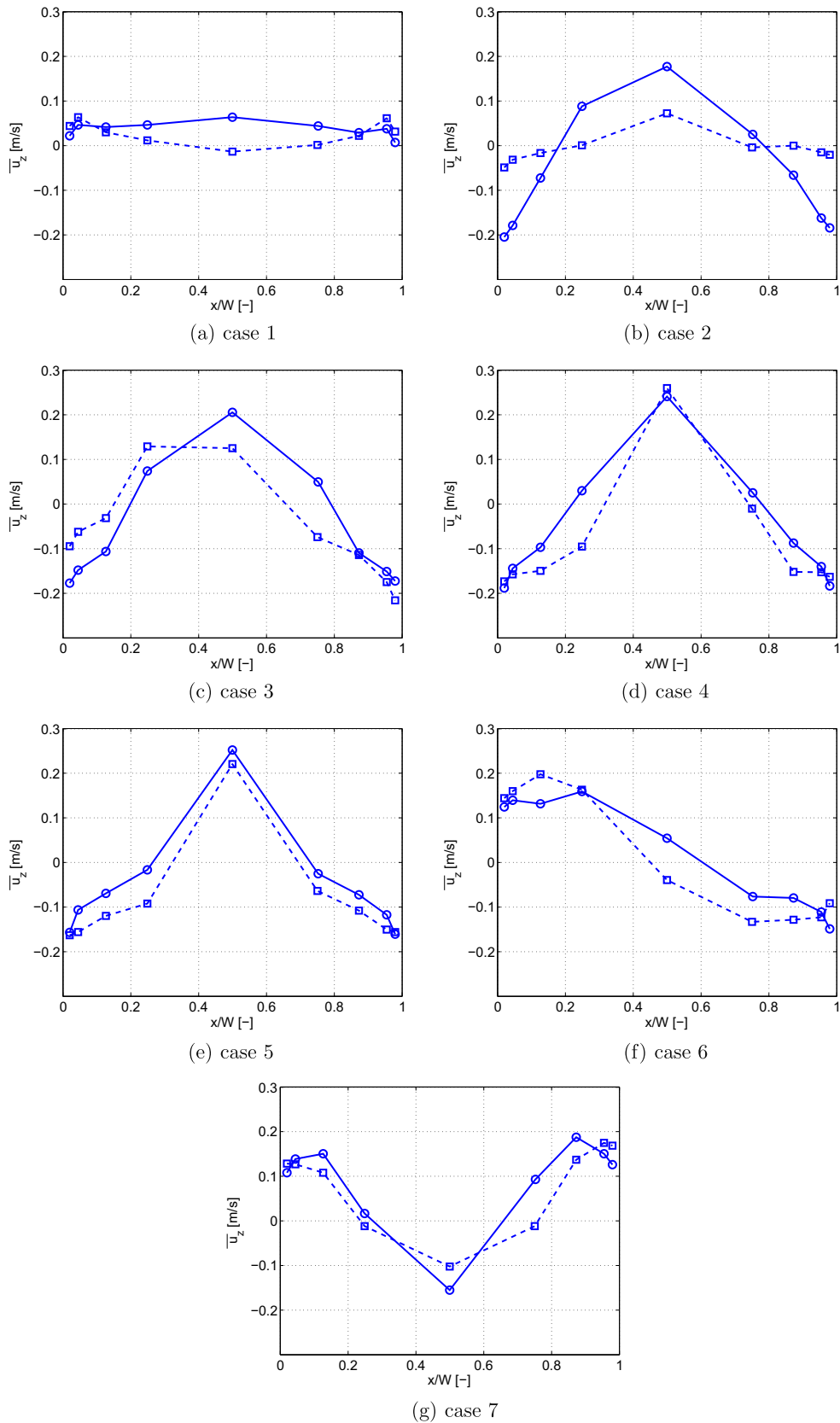
Fig. 17. Axial velocity profiles for various gas injection patterns at $z = 0.05$ m. Continuous line: simulation, dashed line: experiment.

profiles are obtained. In case 1 a relatively flat velocity profile is found, while cases 2–5 show an upflow in the center region and downflow close to the walls. For case 6 an asymmetric velocity profile is present due to the asymmetric aeration. Here, the left part of the column displays upflow, while the right part shows downflow. Finally, for case 7 we found upflow on both sides of
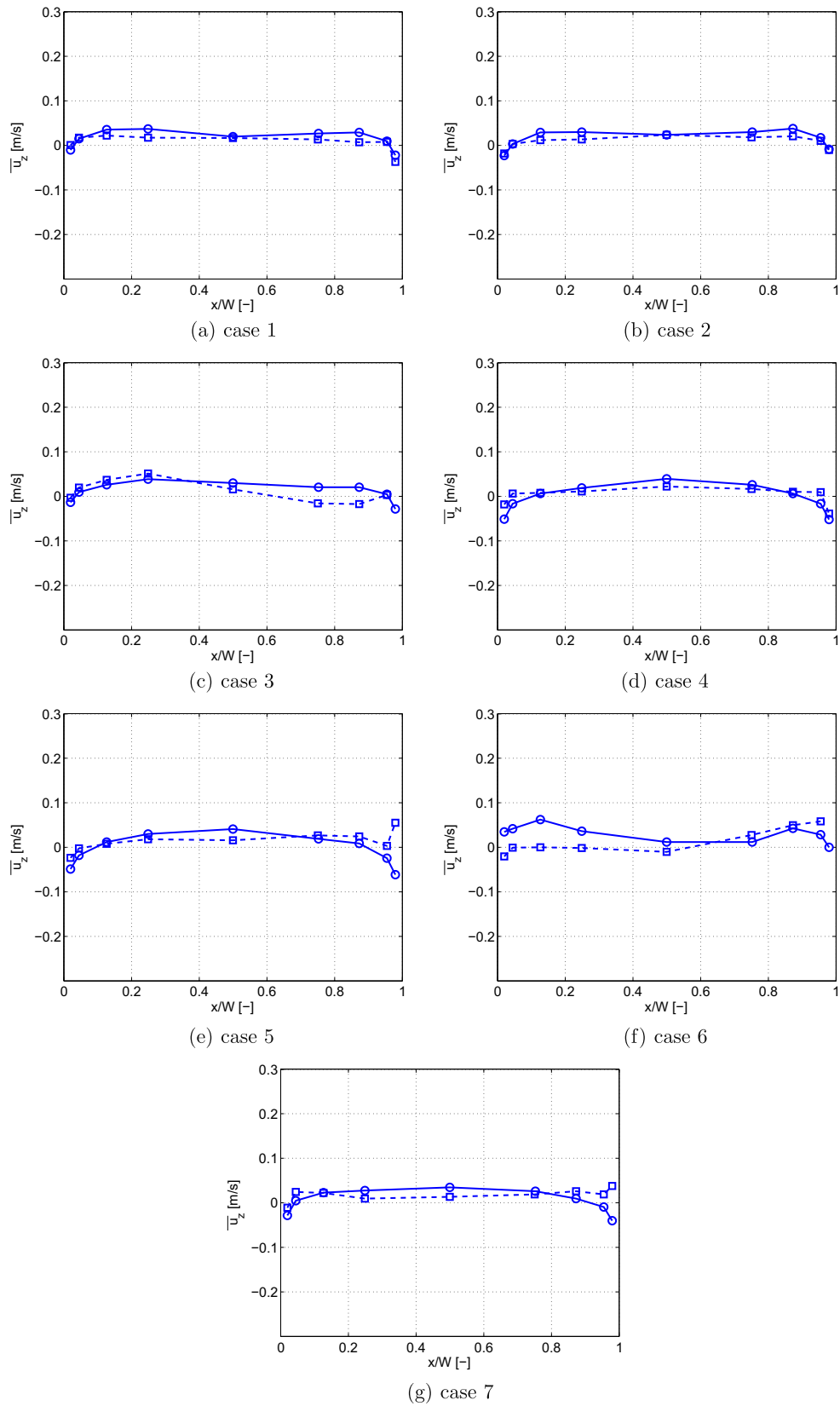
Fig. 18. Axial velocity profiles for various gas injection patterns at $z = 0.7$ m. Continuous line: simulation, dashed line: experiment.

the wall and downflow in the center region. Comparison between experiment and simulation shows that for all cases the velocity profile has been correctly predicted by the present model. Some

discrepancy is found in all cases, but the main patterns are the same. For case 2 however we found that the discrepancy is relatively large compared with the other cases. This is due to the fact
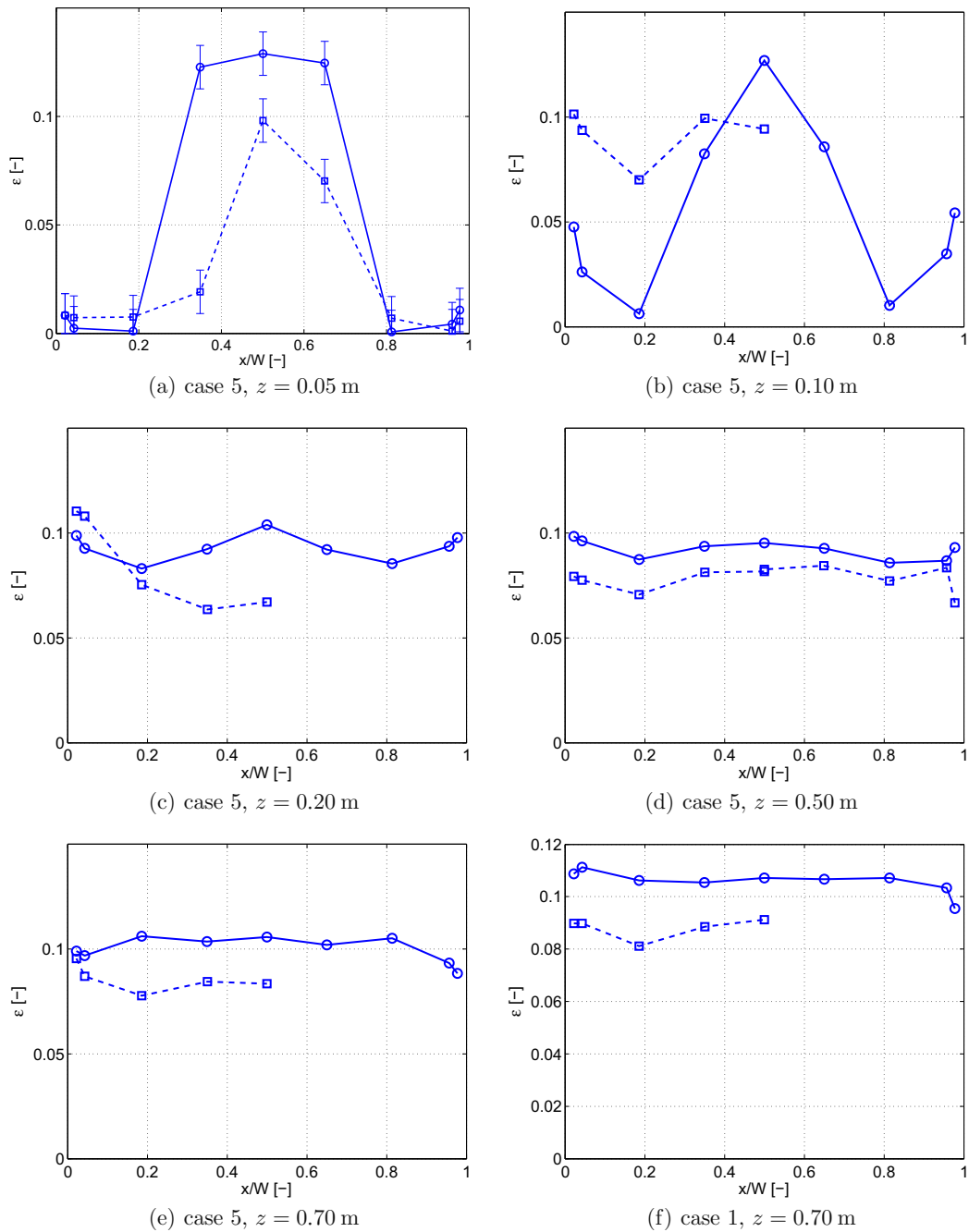
Fig. 19. Void fraction profiles for cases 1 and 5, over the line $y = 0$. Continuous line: simulation, dashed line: experiment. Error bars are shown for $z = 0.05$ m only. For the other plots the error bars have a similar magnitude.

that the simulation overpredicts the vortices in the non-aerated zone as shown in Fig. 9.

For all cases velocity profiles in the higher region of the column (i.e. $z = 0.7$ s) are presented in Fig. 18. At this height we found that the averaged velocity profile is relatively flat for all cases. The strong upflow found at the lower height in cases 2–5 is no longer present, which indicates that the flow is moving rather uniformly close to the column surface. A similar situation is found in cases 6 and 7, where the asymmetric flow found in the bottom section of the column has disappeared. The results indicate that for all cases the predicted velocity profile agrees well with the experimental data. Average void fraction profiles for cases 1 and 5 are shown in Fig. 19. In the top region (i.e. $z \geqslant 0.2$ m), almost no dif-

ference between cases 1 and 5 is found. However, closer to the bottom case 5 shows that the gas hold-up is peaking in the center region and is close to zero on both sides close to the wall. Furthermore, we found that the transition from a bubble plume structure present in the lower part of the column to the homogeneous bubble structure predicted by the present model appears to develop in a higher region compared to the experimental data. When comparing the simulation and experimental results, we find that in general the simulation overpredicts the gas hold-up by about 20%, which is consistent with the integral gas hold-up overprediction described in Section 5.3.

The dynamic behavior is studied via the axial normal stresses. Fig. 20 shows these stresses at various heights and for various
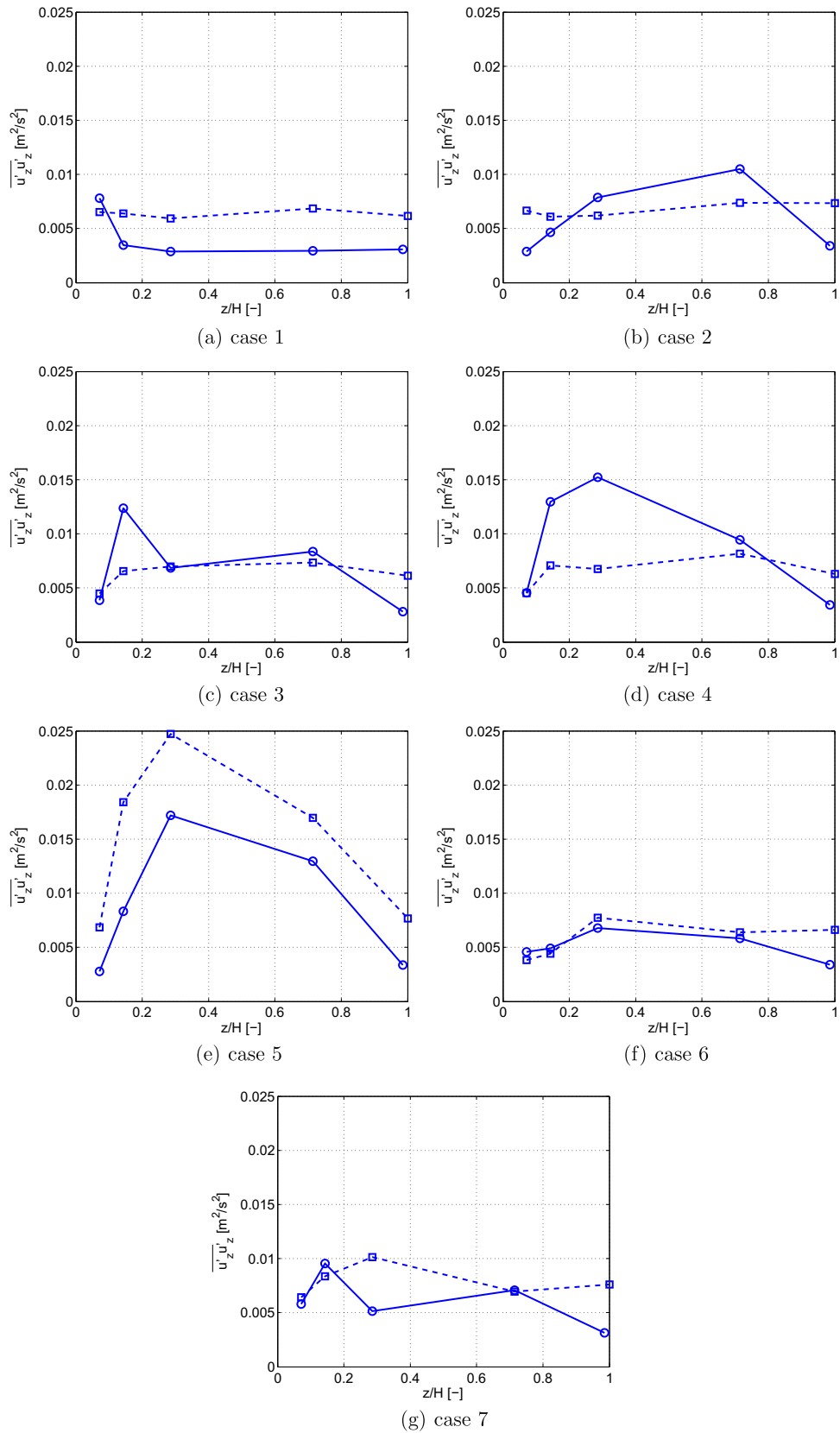
Fig. 20. Axial normal stresses for the various injection patterns. Continuous line: simulation, dashed line: experiment.

injection patterns. As can be seen in the experimental data, the stress level is relatively low for all cases except for case E5, where the flow becomes highly dynamic marked by high stress levels in almost the entire column. In the simulation the results are slightly different; here we found that for all cases the stress level is low, except for case S3, where a significant degree of fluctuation is present

close to the inlet region. A high degree of fluctuation in the entire column is found in cases S4 and S5. Compared to case S4 however, case S5 shows a significantly higher stress level. These results show that the transition from a stable to a dynamic flow condition occurs earlier in the simulation compared with the experiment, which indicates that the present model overpredicts the dynamic behavior of the column. We generally observe that it is harder to describe uniform flow than flow with large vortical structures. Although the applied turbulence model was derived for single phase flow conditions this might be an indication that it performs reasonably well. However, in the absence of large structures, details like slip velocities and bubble path dispersion may be much more sensitive and require more tuning to the specific conditions of the experiment – Tomiyama's models are rather general and do not allow e.g. for the exact level of contamination present in the experiments of Harteveld et al. (2004) that are compared with. Furthermore, due to the flat geometry of the column, the walls have a profound influence on the prevailing hydrodynamics. This is reflected in the small values of the quadratic bubble-to-wall distance D_{bw}^2 and the associated large wall force. Consequently, the results are very sensitive to the applied wall force model. Further work on the validation and improvement of wall force models would be required to treat this aspect more accurately.

6. Conclusions

In this paper, the discrete bubble model is validated against the experimental data of Harteveld et al. (2004) where seven injection patterns are studied to investigate their influence on the flow structure. We found that the model in general is able to reproduce the observed variations rather well. It is found that small deviations from a homogeneous gas distribution at the inlet give rise to the transition to a persistent dynamic flow displaying large convection roles. Only when the gas is introduced homogeneously, the flow stays homogeneous.

For all the studied cases the present model overpredicts the integral gas hold-up by almost 25%. This can most probably be attributed to an overprediction of the drag force, which is a result of various factors, such as competing hindrance and cooperative rise effects, as well as the level of contamination in the fluid. Despite this systematic overprediction, the trends of the change in gas hold-up agree very well with the experiment. The velocity profiles in general agree with the experiment, however we have noticed that the simulation results tend to produce stronger upflow in the center of the column and stronger downflow close the walls. We suspect that this behavior is due to the fact that in the experiments the liquid is moving in between the bubbles while in the simulation the liquid moves in a large circulation pattern, because the details at the scale of the bubble cannot be resolved due to the nature of the model. Finally, the simulations display an earlier transition from the stable to the dynamic regime compared with the experimental data, which might result from an inaccuracy of the turbulence model at high gas hold-ups. Further study to investigate the validity of the turbulence model at high gas hold-ups is necessary.

References

Becker, S., Sokolichin, A., Eigenberger, G., 1994. Gas–liquid flow in bubble columns and loop reactors: Part II. Comparison of detailed experiments and flow simulations. Chem. Eng. Sci. 49, 5747–5762.

Behzadi, A., Issa, R.I., Rusche, H., 2004. Modelling of dispersed bubble and droplet flow at high phase fractions. Chem. Eng. Sci. 59, 759–770.

Borchers, O., Busch, C., Sokolichin, A., Eigenberger, G., 1999. Applicability of the standard k–ϵ turbulence model to the dynamic simulation of bubble columns. Part II: Comparison of detailed experiments and flow simulations. Chem. Eng. Sci. 54, 5927–5935.

Buwa, V.V., Ranade, V.V., 2003. Mixing in bubble columns reactors: role of unsteady flow structures. Can. J. Chem. Eng. 81, 402–411.

Buwa, V.V., Deo, D.S., Ranade, V.V., 2006. Eulerian–Lagrangian simulations of unsteady gas-liquid flows in bubble columns. Int. J. Multiphase Flow 32, 864–885.

Cartellier, A., 1992. Simultaneous void fraction measurement, bubble velocity and size estimates using a single optical probe in gas–liquid two-phase flows. Rev. Sci. Instrum. 63, 5442–5453.

Centrella, J., Wilson, J.R., 1984. Planar numerical cosmology. II. The difference equations and numerical tests. Astron. Astrophys. J. Suppl. Ser. 54, 229–249.

Chen, P., Dudukovic, M.P., Sanyal, J., 2005a. Three-dimensional simulation of bubble column flows with bubble coalescence and breakup. AIChE J. 51, 696–712.

Chen, P., Sanyal, J., Dudukovic, M.P., 2005b. Numerical simulation of bubble columns flows: effect of different breakup and coalescence closures. Chem. Eng. Sci. 60, 1085–1101.

Darmana, D., Deen, N.G., Kuipers, J.A.M., 2004. Modelling of mass transfer and chemical reactions in a bubble column reactor using a discrete bubble model. In: Proceedings of the 5th International Conference on Multiphase Flow, Yokohama, Japan. Paper No. 328.

Darmana, D., Deen, N.G., Kuipers, J.A.M., 2005a. Detailed modelling of hydrodynamics, mass transfer and chemical reactions in a bubble column using a discrete bubble model. Chem. Eng. Sci. 60, 3383–3404.

Darmana, D., Henket, R.L.B., Deen, N.G., Kuipers, J.A.M., 2005b. Experimental and numerical investigations of a chemisorption process in a bubble column reactor. In: Proceedings of the 7th World Congress of Chemical Engineering, Glasgow, Scotland, UK.

Darmana, D., Deen, N.G., Kuipers, J.A.M., 2006. Parallelization of an Euler–Lagrange model using mixed domain decomposition and mirror domain technique: application to dispersed gas-liquid two-phase flow. J. Comput. Phys. 220, 216–248.

Darmana, D., Henket, R.L.B., Deen, N.G., Kuipers, J.A.M., 2007. Detailed modelling of hydrodynamics, mass transfer and chemical reactions in a bubble column using a discrete bubble model: chemisorption of CO_2 into NAOH solution, numerical and experimental study. Chem. Eng. Sci. 62, 2556–2575.

Deen, N.G., Solberg, T., Hjertager, B.H., 2001. Large eddy simulation of the gas–liquid flow in a square cross-sectioned bubble column. Chem. Eng. Sci. 56, 6341–6349.

Deen, N.G., Annaland, M.V.S., Kuipers, J.A.M., 2004. Multi-scale modeling of dispersed gas–liquid two-phase flow. Chem. Eng. Sci. 59, 1853–1861.

Delnoij, E., Lammers, F.A., Kuipers, J.A.M., van Swaaij, W.P.M., 1997. Dynamic simulation of dispersed gas-liquid two-phase flow using a discrete bubble model. Chem. Eng. Sci. 52, 1429–1458.

Delnoij, E., Kuipers, J.A.M., Swaaij, W.P.M.V., 1999. A three-simensional CFD model for gas–liquid bubble columns. Chem. Eng. Sci. 54, 2217–2226.

Harteveld, W.K., 2005. Bubble Columns – Structures or Stability? Ph.D. thesis. Delft University of Technology, The Netherlands.

Harteveld, W.K., Julia, J.E., Mudde, R.F., van den Akker, H.E.A., 2004. Large scale vortical structures in bubble columns for gas fractions in the range of 5–25%. In: Proceedings of CHISA 16th International Congress Of Chemical And Process Engineering, Prague, Czech Republic.

Hoomans, B.P.B., Kuipers, J.A.M., Briels, W.J., Swaaij, W.P.M.V., 1996. Discrete particle simulation of bubble and slug formation in a two-dimensional gas–fluidised bed: a hard-sphere approach. Chem. Eng. Sci. 51, 99–118.

Julia, J.E., Harteveld, W.K., Mudde, R.F., den Akker, H.E.A.V., 2005. On the accuracy of the void fractione measurements using optical probes in bubbly flows. Rev. Sci. Instrum. 76.

Kuipers, J.A.M., van Duin, K.J., van Beckum, F.P.H., van Swaaij, W.P.M., 1993. Computer simulation of the hydrodynamics of a two dimensional gas–fluidized bed. Comput. Chem. Eng. 17, 839–858.

Laín, S., Bröder, D., Sommerfeld, M., 1999. Experimental and numerical studies of the hydrodynamics in a bubble column. Chem. Eng. Sci. 54, 4913–4920.

Laín, S., Bröder, D., Sommerfeld, M., Göz, M.F., 2002. Modelling hydrodynamics and turbulence in a bubble column using the Euler–Lagrange procedure. Int. J. Multiphase Flow 28, 1381–1407.

Monahan, S.M., Vitankar, V.S., Fox, R.O., 2005. Cfd predictions for flow-regime transitions in bubble columns. AIChE J. 51, 1897–1923.

Mudde, R.F., Saito, T., 2001. Hydrodynamical similarities between bubble column and pipe flow. J. Fluid Mech. 437, 203–228.

Mudde, R.F., Simonin, O., 1999. Two- and three-dimensional simulations of a bubble plume using a two-fluid model. Chem. Eng. Sci. 54, 5061–5069.

Oey, R.S., Mudde, R.F., Van den Akker, H.E.A., 2003. Sensitivity study on interfacial closure laws in two-fluid bubbly flow simulations. AIChE J. 49, 1621–1636.

Patankar, S.V., Spalding, D.B., 1972. A calculation procedure for heat, mass and momentum transfer in three-dimensional parabolic flows. Int. J. Heat Mass Transfer 15, 1787–1806.

Sokolichin, A., Eigenberger, G., 1999. Applicability of the standard k–ϵ turbulence model to the dynamic simulation of bubble columns: Part I. Detailed numerical simulations. Chem. Eng. Sci. 54, 2273–2284.

Sokolichin, A., Eigenberger, G., Lapin, A., Lübbert, A., 1997. Dynamic numerical simulation of gas–liquid two-phase flows: Euler/Euler versus Euler/Lagrange. Chem. Eng. Sci. 52, 611–626.

Sokolichin, A., Eigenberger, G., Lapin, A., 2004. Simulation of buoyancy driven bubbly flow: established simplifications and open questions. AIChE J. 50, 24–45.

Tomiyama, A., Matsuoka, T., Fukuda, T., Sakaguchi, T., 1995. A simple numerical method for solving an incompressible two-fluid model in a general curvilinear coordinate system. In: Serizawa, A., Fukano, T., Bataille, J. (Eds.), Advances in Multiphase Flow. Society of Petroleum Engineers, Inc., Elsevier, Amsterdam, pp. 241–252.

Tomiyama, A.I., Zun, H.H., Makino, Y., Sakaguchi, T., 1997. A three-dimensional particle tracking method for bubbly flow simulation. Nucl. Eng. Des. 175, 77–86.

Tomiyama, A., Tamai, H., Zun, I., Hosokawa, S., 2002. Transverse migration of single bubbles in simple shear flows. Chem. Eng. Sci. 57, 1849–1858.

van den Hengel, E.I.V., Deen, N.G., Kuipers, J.A.M., 2005. Application of coalescence and breakup models in a discrete bubble model for bubble columns. Ind. Eng. Chem. Res. 44, 5233–5245.

Vreman, A.W., 2004. An eddy-viscosity subrid-scale model for turbulent shear flow: algebraic theory and applications. Phys. Fluids 16, 3670–3681.